

1 Migrating diurnal tide anomalies during QBO disruptions in 2016 and 2 2020: morphology and mechanism

3 Shuai Liu^{1,2}, Guoying Jiang^{1,3,4}, Bingxian Luo^{1,2}, Xiao Liu⁵, Jiyao Xu^{1,3}, Yajun Zhu^{1,3,4}, Wen Yi^{6,7}

4 ¹State Key Laboratory of Solar Activity and Space Weather, National Space Science Center, Chinese Academy of Sciences,
5 Beijing, 100190, China

6 ²College of Earth and Planetary Sciences, University of Chinese Academy of Sciences, Beijing, 101408, China

7 ³School of Astronomy and Space Science, University of Chinese Academy of Sciences, Beijing, 101408, China

8 ⁴Hainan National Field Science Observation and Research Observatory for Space Weather, Danzhou, Hainan Province, China.

9 ⁵School of Mathematics and Statistics, Henan Normal University, Xinxiang, 453007, China

10 ⁶CAS Key Laboratory of Geospace Environment, Department of Geophysics and Planetary Sciences, University of Science
11 and Technology of China, Hefei, China

12 ⁷CAS Center for Excellence in Comparative Planetology, Anhui Mengcheng Geophysics National Observation and Research
13 Station, University of Science and Technology of China, Hefei, China

14 *Correspondence to:* Guoying Jiang (gyjiang@swl.ac.cn) and Bingxian Luo (luobx@nssc.ac.cn)

15 **Abstract.** The stratosphere Quasi-Biennial Oscillation (QBO) modulates the migrating diurnal tide (DW1) in the mesosphere
16 and lower thermosphere (MLT). DW1 amplitudes are larger during QBO westerly (QBOW) than during easterly (QBOE)
17 phases. Since QBO's discovery in 1953, two rare QBO disruption events occurred in 2016 and 2020. During these events,
18 anomalous westerly winds propagate upward, disrupting normal downward propagation of easterly phase and producing a
19 persistent westerly wind layer. In this study, global responses of DW1 amplitudes and phases in MLT to these QBO disruptions,
20 as well as their underlying mechanisms are investigated, using SABER/TIMED observations, MERRA-2 reanalysis and SD-
21 WACCM-X simulations. Similarity of the DW1 responses to these two events is that DW1 phases and wavelengths exhibit
22 close results to QBOW, whereas amplitudes lie between QBOW and QBOE. DW1 amplitudes in equatorial MLT (maximum
23 difference) vary by 20.5% and -10.2% relative to QBOE and QBOW in 2016 event, but by 6.0% and -21.1% in 2020 event.
24 In 2016 event, water-vapor radiative and latent heating, jointly modulated by the event and ENSO, increase significantly
25 relative to QBOE. Less dissipation and less tidal energy removal in stratosphere along with gravity-wave (GW) drag in
26 mesosphere tend to enhance DW1 amplitudes. In contrast, in 2020 event, water-vapor heating exhibits a 5% increase. The
27 dissipation and tidal energy removal has adverse effect on DW1, while GW drag exerts a weaker influence. The enhancement
28 of water vapor heating together with the weaker GW drag likely accounts for the weaker enhancement of DW1 during this
29 event.

30

31 1 Introduction

32 Atmospheric solar tides are planetary-scale harmonic waves with periods of a solar day. In the mesosphere and lower
33 thermosphere (MLT), solar tides exert significant influences on atmospheric parameters such as wind, temperature, and density
34 (Chapman & Lindzen, 1980; Xu et al., 2009; Jiang et al., 2010; Smith, 2012). Among these tides, the migrating diurnal tide
35 (DW1) is one of the most prominent components. DW1 in MLT is modulated by external forcings, including the stratosphere
36 Quasi-Biennial Oscillation (QBO, Hagan et al., 1999; Wu et al., 2008; Xu et al., 2009; Oberheide et al., 2009; Mukhtarov et
37 al., 2009; Davis et al., 2013; Gan et al. 2014), El Niño–Southern Oscillation (ENSO, Lieberman et al., 2007; Cen et al., 2022)
38 and 11-year solar cycle response (Singh and Gurubaran, 2017; Sun et al., 2022; Liu et al., 2024a; Liu et al., 2024b). In this
39 work, the impact of QBO is focused on.

40 The QBO dominates the variability of the equatorial stratosphere (~ 16 – 50 km), shown as alternating downward propagating
41 easterly wind (so-called QBO easterly phases) and westerly wind (so-called QBO westerly phases), with an averaging period
42 of approximately 28 months (Baldwin et al., 2001). QBO is driven by vertically propagating Kelvin waves, mixed Rossby
43 gravity waves and small-scale gravity waves (Lindzen and Holton, 1968; Holton and Lindzen, 1972; Baldwin et al., 2001; Ern
44 et al., 2014). It could influence the transport and distribution of trace gases like water vapor and ozone in the troposphere and
45 stratosphere (Schoeberl et al., 2008).

46 During the winter of 2015/16 and 2019/20, two rare stratospheric QBO disruption events occurred, which were found only
47 twice since the record began in 1953. The events are manifested by anomalous westerly winds propagating upward, disrupting
48 normal downward propagation of the easterly phase and producing a persistent westerly wind layer (Newman et al., 2016;
49 Anstey et al., 2021). The 2016 QBO disruption has been confirmed to have a close causal relationship with the 2015/16 extreme
50 El Niño event (Newman et al., 2016; Osprey et al., 2016; Barton and McCormack, 2017; Coy et al., 2017). The 2015/16 El
51 Niño substantially weakened the subtropical easterly jet, allowing enhanced Rossby wave propagation from the extratropics
52 into the deep tropics near 40 hPa (Barton and McCormack, 2017). These amplified Rossby waves subsequently broke and
53 deposited momentum near the QBO westerly core, rather than at the climatological zero-wind line, causing a pronounced
54 deceleration. The deceleration gave rise to a persistence of westerlies at 40–15 hPa, preventing the expected transition to
55 easterlies and ultimately leading to the QBO disruption (Newman et al., 2016; Osprey et al., 2016; Coy et al., 2017; Barton
56 and McCormack, 2017; Kang et al., 2022; Wang et al., 2023). The QBO disruption was accompanied by a marked
57 strengthening of the Brewer–Dobson residual circulation, thereby intensifying tropical upwelling. This upwelling contributed
58 to an upward displacement of westerlies in the tropical lower stratosphere (Coy et al., 2017), modifying the transport and
59 distribution of trace gases such as water vapor. The persistent westerlies also created conducive background conditions for the
60 vertical propagation of DW1. Nevertheless, not all strong El Niño events trigger QBO disruptions. In the 2015/16 case, the
61 QBO westerly wind core was weaker and Rossby wave activity was stronger than in other extreme events, such as the 1998
62 El Niño (Barton and McCormack, 2017). In the 2020 event, the upward-propagating westerly wind was so weak that the
63 monthly mean zonal wind appeared as upward-propagating easterly wind (e.g., Anstey et al., 2021; Wang et al., 2023). This

64 event was driven by strong extratropical Rossby waves associated with the 2019 minor SSW in the southern hemisphere (Kang
 65 and Chun, 2021; Wang et al., 2023). In these two events, the trace gases such as ozone and water vapor are modulated. During
 66 the 2016 QBO disruption event, positive water vapor anomalies were observed between the tropopause and lower stratosphere,
 67 while positive ozone anomalies appeared in the upper stratosphere (Tweedy et al., 2017; Diallo et al., 2018). A similar pattern
 68 was reported for the 2020 disruption event, with water vapor in the lower stratosphere and ozone in the upper stratosphere also
 69 exhibiting positive anomalies (Diallo et al., 2022).

70 QBO modulation of diurnal tides has been reported by both ground-based and space-borne observations (Araújo et al., 2017;
 71 Davis et al., 2013; Pramitha et al., 2021b; Wu et al., 2008; Dhadly et al., 2018). Mayr and Mengel (2005) reported that the
 72 QBO can affect these amplitudes by up to 30% using the Numerical Spectral Model (NSM). Thermosphere, Ionosphere,
 73 Mesosphere Energetics and Dynamics/Sounding of the Atmosphere using Broadband Emission Radiometry (TIMED/SABER)
 74 observations revealed that the quasi-biennial variability of DW1 could exceed 50% at certain altitudes (Garcia, 2023). The
 75 modulation was characterized by larger-than-average diurnal tide amplitudes during the westerly phase of the QBO and
 76 smaller-than-average amplitudes during the easterly phase (Vincent et al., 1998; Wu et al., 2008; Xu et al., 2009; Davis et al.,
 77 2013; Araújo et al., 2017; Pramitha et al., 2021b; Garcia, 2023). Several mechanisms have been proposed for modulating the
 78 migrating diurnal tide (DW1). A primary factor emphasized in many studies is the variation in the background zonal wind and
 79 its latitudinal shear (Forbes and Vincent, 1989; Hagan et al., 1999; McLandress, 2002b; Riggin and Lieberman, 2013; Liu et
 80 al., 2015; Ortland, 2017; Dhadly et al., 2018; Pramitha et al., 2021a, b). Forbes and Vincent (1989) demonstrated that the DW1
 81 (1,1) mode experiences stronger dissipation in easterly phases than in westerly phases, while McLandress (2002b) highlighted
 82 the tide's strong sensitivity to latitudinal shears in the zonal mean easterlies of the summer mesosphere. Apart from the
 83 influence of the background wind, additional contributions have been suggested, including variations in diurnal heating
 84 (McLandress, 2002b; Riggin and Lieberman, 2013; Ortland, 2017) and tide-gravity wave (GW) interactions (Mayr et al., 1998;
 85 McLandress, 2002a; Lu et al., 2012; Wang et al., 2024), both of which may play a role in modulating the QBO-related
 86 variability of DW1.

87 Recent studies have shown that the diurnal tides were modulated during the QBO disruption events (Pramitha et al., 2021a;
 88 Garcia, 2023; Wang et al., 2024). Pramitha et al. (2021a) first reported the enhancement of the diurnal tides during the
 89 2015/2016 QBO disruption event using a meteor radar over Tirupati (13.63°N, 79.4°E) and linked this enhancement to changes
 90 in ozone concentration. Garcia (2023) showed the equatorial response of temperature DW1 to these two disruption events
 91 when analysing the QBO modulation to DW1. Wang et al. (2024) reported the weakened mesospheric diurnal tides at mid-
 92 latitude during QBO disruption events, which were observed by a meteor radar chain. They further provided the modulation
 93 evidence of gravity wave forcing and solar radiative absorption by subtropical stratospheric ozone, as revealed by SD-
 94 WACCM-X simulations.

95 These findings raise three questions: (1) In addition to the equatorial peak, temperature DW1 exhibits secondary amplitude
 96 maxima at 30°N and 30°S (Xu et al., 2009; Garcia, 2023). Whether the DW1 amplitudes on a global scale show a similar
 97 response to the QBO disruption events. (2) Whether the phases and wavelengths of DW1 could be affected by the events. (3)

98 Mechanisms for modulating DW1 include heating sources such as water vapor radiative heating and latent heating, zonal wind
99 latitudinal shear, and tide-gravity wave interactions (e.g., Forbes and Vincent, 1989; Hagan, 1996; Hagan et al., 1999;
100 McLandress, 2002a; Kogure and Liu, 2021). Whether these mechanisms play significant roles in modulating DW1 during
101 QBO disruption events.

102 The present study will focus on the global response feature of DW1 and its underlying mechanisms to QBO disruption events.
103 The response of DW1 amplitudes, phases and wavelengths during the event will be investigated. Moreover, the contribution
104 of possible mechanisms, including heating sources, the zonal wind latitudinal shear and tidal-gravity wave interaction during
105 the event, will be explored. The article is organized as follows: Section 2 introduces TIMED/SABER, SD-WACCM-X, and
106 MERRA-2 data and the methodologies to extract the migrating tides. Section 3 presents the response feature of the DW1 to
107 the QBO disruption events revealed by SABER/TIMED observations and SD-WACCM-X simulation results. The possible
108 mechanism of DW1 response to the disruption events is discussed in Section 4. Section 5 presents the summary.

109 **2 Data and methodology**

110 This study employs the dataset of SABER/TIMED observations, SD-WACCM-X simulations and MERRA-2 reanalysis to
111 reveal the feature of DW1 and its excitation sources during QBO disruption events. DW1 amplitude, phase, and wavelength
112 are derived from both SABER/TIMED data and SD-WACCM-X outputs. MERRA-2 reanalysis is used to analyse the
113 contributions of water vapor radiative heating and latent heating to DW1 variability during the QBO disruption events, while
114 SABER/TIMED observations characterize ozone radiative heating. SD-WACCM-X simulations validate the excitation source
115 revealed by the observational datasets.

116 **2.1 SABER/TIMED observations**

117 The TIMED satellite is in a near sun-synchronous orbit with a 73° inclination at about 625 km. The number of orbits observed
118 per day is about 15. SABER, an instrument in the TIMED satellite, is a 10-channel broadband (1.27–17 μm) limb-scanning
119 infrared radiometer. SABER observations of infrared radiance are used to retrieve kinetic temperature, trace gases, etc. In this
120 work, kinetic temperature and ozone observations in level 2 A (L2A) dataset and ozone heating rate in level 2B (L2B) dataset
121 are selected to analyse the DW1 response to QBO disruption events. Kinetic temperature is derived using a full nonlocal
122 thermodynamic equilibrium (non-LTE) inversion algorithm (Mertens et al., 2001; 2004) with the combination of the measured
123 15 μm CO_2 vertical emission profile and CO_2 concentrations provided by the Whole Atmosphere Community Climate Model
124 (WACCM 3.5.48), as described by Garcia et al. (2007).

125 It takes SABER 60 days to sample 24 hours in local time. The data latitudinal coverage every 60 days extends from 53°N to
126 83°S or 53°S – 83°N . Temperature observations taken from version 2.07 data from 2002 to 2019 and version 2.08 data from
127 2020 to 2023 are used. The details of the version switches could refer to Mlynczak et al. (2022, 2003). The retrieved
128 temperature observations used in this work cover altitudes from approximately 15 km to 105 km.

129 **2.2 SD-WACCM-X**

130 The Whole Atmosphere Community Climate Model with thermosphere–ionosphere eXtension (WACCM-X) is a
131 comprehensive numerical model that could simulate the Earth's atmosphere from the surface up to the upper thermosphere
132 (~500–700 km), including the ionosphere (Liu et al., 2010; 2018). WACCM-X is a single, unified whole-atmosphere model
133 that extends the NCAR Whole Atmosphere Community Climate Model (WACCM4; Marsh et al., 2013). WACCM4 itself was
134 built upon the Community Atmosphere Model 4 (CAM4; Neale et al., 2013). While the thermosphere–ionosphere physics
135 (e.g., global electrodynamics, O^+ transport, electron/ion energetics) incorporated in WACCM-X were largely adapted from the
136 NCAR Thermosphere–Ionosphere–Electrodynamics General Circulation Model (TIE-GCM; Qian et al., 2014; Pedatella,
137 2022), they have been re-engineered within the WACCM-X dynamical core and coupled to the lower- and middle-atmosphere
138 processes through a dedicated ionosphere-interface module. SD in the SD-WACCM-X means specified dynamics, which is
139 an approach described in Smith et al. (2017). The reanalysis fields from Modern-Era Retrospective analysis for Research and
140 Applications, Version 2 (MERRA-2, Gelaro et al., 2017) data from the surface up to ~50 km are nudged in WACCM-X.
141 Model parameters are output in 3-hour resolution. The latitude-longitude resolution is $1.9^\circ \times 2.5^\circ$. The model has 145 pressure
142 levels with a varying vertical resolution of ~1.1–1.75 km in the troposphere and stratosphere and ~3.5 km in the mesosphere.
143 In this work, the temperature, zonal wind, temperature tendency due to moist process and long wave heating rate ranging from
144 2002 to 2022 are selected.

145 **2.3 MERRA-2**

146 MERRA-2 is a reanalysis product from the NASA Global Modeling and Assimilation Office (GMAO) and provides data like
147 wind, temperature, mixing ratio of components, and so on. (Gelaro et al., 2017). In this work, the zonal wind, temperature, air
148 density, surface albedo, water vapor mixing ratio and temperature tendency due to moist process range from 2002 to 2023 are
149 selected. The time resolution is 3-hour per day. The spatial resolution is a $2.5^\circ \times 2.5^\circ$ latitude-by-longitude grid at 72 model
150 levels from ground to 0.01 hPa.

151 **2.4 Singapore radiosonde QBO index**

152 The QBO index employed in this study is derived from Singapore radiosonde measurements obtained by the Meteorological
153 Service Singapore Upper Air Observatory (station 48698; 1.34°N , 103.89°E ; 21 m above mean sea level). The monthly mean
154 zonal wind data processed by the National Aeronautics and Space Administration/Goddard Space Flight Center (NASA/GSFC)
155 is selected, spanning 2002–2023 at pressure levels between 100 hPa and 10 hPa.

156 **2.5 Water vapor radiative heating rate calculation**

157 Troposphere heating by water vapor absorption of near-infrared radiation is an important excitation source for DW1 (Hagan,
158 1996; Lieberman et al., 2003). Due to the SABER's observational gap in the troposphere, the MERRA-2 dataset is adopted.

159 In this dataset, temperature, air density, surface albedo, cloud fraction and water vapor mixing ratio (specific humidity) are the
 160 variables necessary for the calculation. The heating rate is the sum of clear sky and cloudy sky (Groves et al., 1982):
 161
$$J = (1 - k)J_{clear} + kJ_{cloudy} \quad (1)$$

 162 where k is the cloud fraction, J_{clear} and J_{cloudy} are the heating rates of the clear sky and cloudy sky. The calculation equations
 163 for clear sky and cloudy sky are given in Appendix A.

164 2.6 Ozone radiative heating rate calculation

165 The calculation of ozone radiative heating follows the Strobel/Zhu scheme (Strobel, 1978; Zhu, 1994), in which the total
 166 heating rate is obtained as the sum of contributions from the Hartley, Huggins, and Chappuis bands, with parameterizations
 167 from Zhu (1994). The required ozone volume mixing ratio (VMR) and density are taken from the SABER L2A dataset. Ozone
 168 VMR is retrieved from vertical emission profiles at 9.6 μm and 1.27 μm (Smith et al., 2013). The former covers all local times
 169 and the latter is limited to daytime. In this study, the 9.6 μm retrievals are used. It should be noted that the Strobel/Zhu model
 170 omits the dominant nighttime chemical-heating source between ~ 70 and 100 km (Zhu, 1994; Xu et al., 2010). Consequently,
 171 the present analysis is restricted to the sum of the three-band heating rates between 20 and 70 km.

172 2.7 Method for extracting DW1 and data processing

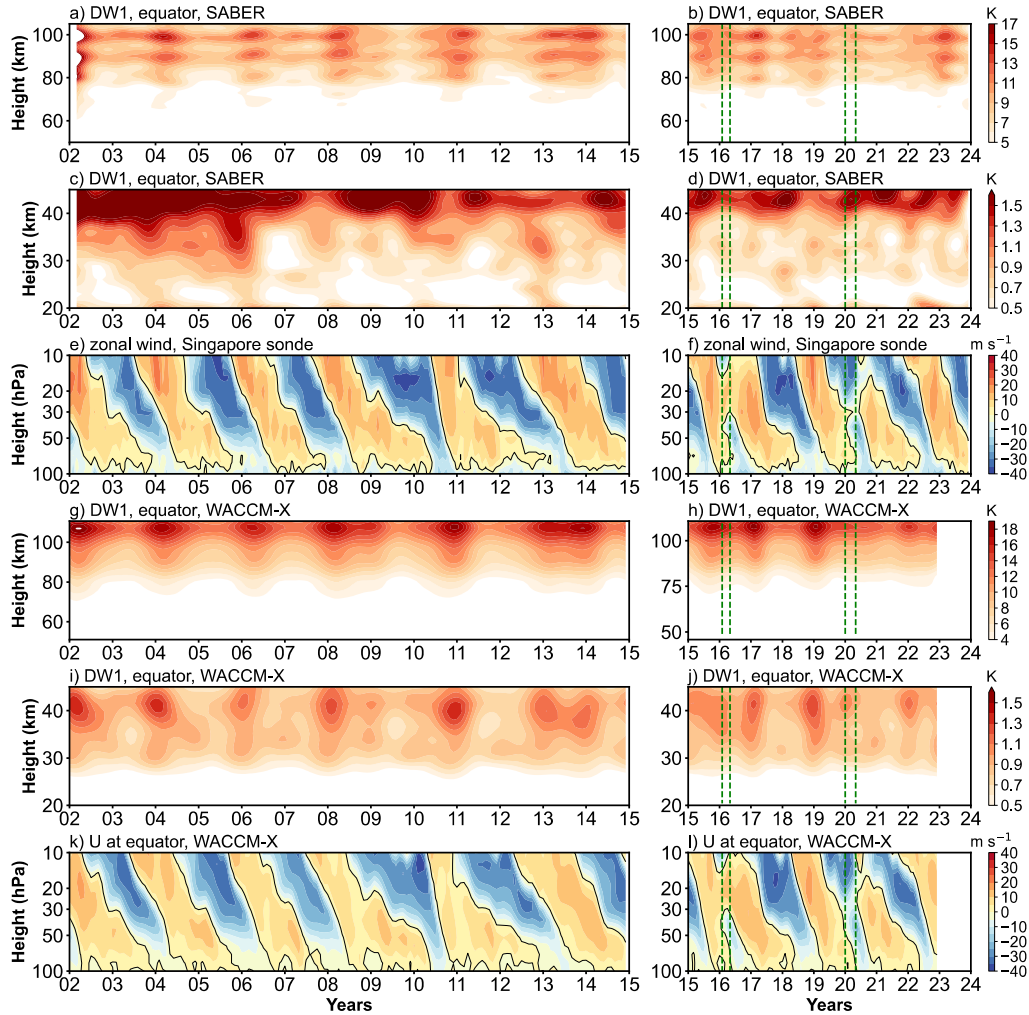
173 Non-uniform SABER observational data were processed into zonal mean data and used to extract tides. The procedures are
 174 briefly introduced as follows. Firstly, the kinetic temperature, ozone mixing ratio and ozone radiative heating rate profiles are
 175 interpolated vertically with a 1 km spacing. Profiles for each day are sorted into ascending and descending groups. Secondly,
 176 the global temperature and ozone observations at whole heights and in both groups were processed into zonal mean results,
 177 covering latitudes from 50°S to 50°N with a resolution of 5°. At a fixed latitude and height, the following equation proposed
 178 by Xu et al. (2007) is used to extract the tide from the zonal mean temperature in a 60-day window:

$$179 \quad \frac{1}{2\pi} \int_0^{2\pi} T(t_{LT}, \lambda) d\lambda = \bar{T} + \eta(t - t_0) + \sum_{n=1}^N A_n \cos(n\omega t_{LT}) + \sum_{n=1}^N B_n \sin(n\omega t_{LT}) \quad (2)$$

180 where $\omega = 2\pi/24$ (hour), t_{LT} is the local time, λ is longitude in radians. \bar{T} is the 60-day window average of the zonal mean
 181 temperature. η describes the linear trend variation in the window. t is the day of the window and t_0 is the center day of
 182 the window. The third and fourth terms of the right section of the equation denotes the superimposed harmonic signals by four
 183 periods migrating tides, including diurnal tide (DW1), semidiurnal tide (SW2), terdiurnal tide (TW3), and 6-h tide (QW4). N
 184 in the third term represents four signals and n denotes each signal. The amplitude and phase of each migrating tide are retrieved
 185 using $\sqrt{A_n^2 + B_n^2}$ and $\arctan(B_n/A_n)$, respectively. The overlapping analyses are obtained by sliding the 60-day window
 186 forward in 1-day intervals to obtain the daily values of the wave characteristics. The details of the methods used for data
 187 processing and tide extraction could refer to Xu et al. (2007, 2009) and Liu et al. (2024a).

188 The method for extracting tidal components from ozone heating rates follows Equation 4 in Xu et al. (2010). The methods for
 189 tidal extraction from MERRA-2 and SD-WACCM-X differ from those used for SABER due to differences in data structure.

190 Unlike SABER, both MERRA-2 and SD-WACCM-X provide spatially uniform data with a 3-hour temporal resolution. As a
191 result, a two-dimensional Fast Fourier Transform (2D-FFT) is directly applied to extract daily DW1 amplitudes and phases of
192 temperature, water vapor heating rate, and temperature tendency due to moist processes. For further analysis, the Hough mode
193 decomposition is applied to the DW1. The program is retrieved from https://github.com/masaru-kogure/Hough_Function. As
194 in Sakazaki (2013), DW1 in the stratosphere can be reasonably well represented by a superposition of only a few (~ 4) Hough
195 modes. Here the (1, -2), (1, -1), (1, 1) and (1, 2) modes are used. The monthly mean temperature DW1 amplitudes obtained
196 from SABER, MERRA-2 and SD-WACCM-X are calculated. Due to the observational gap of SABER, the Generalized Lomb-
197 Scargle Periodogram (from PyAstronomy) is applied to fill the missing data of ozone heating rate. A low-pass Butterworth
198 filter of 3rd order with a cut-off period of 13 months (≈ 0.077 cycles month⁻¹) is applied to reveal the DW1 QBO variations
199 (temperature, ozone heating and so on).



202

203 **Figure 1. (a, b) Low-pass filtered amplitudes (periods longer than 13 months) of the migrating diurnal tide (DW1; monthly mean,**
 204 **in K) as a function of altitude in the mesosphere and lower thermosphere (MLT) and time (2002–2023), derived from**
 205 **SABER/TIMED temperature observations. (c, d) Same as (a, b) but for the stratosphere. (e, f) Zonal wind at the stratospheric**
 206 **equator from Singapore sonde. (g–i) Similar to (a–f), but based on SD-WACCM-X simulations. Vertical green dashed lines indicate**
 207 **the QBO disruption periods in 2015/16 (February–May 2016) and 2019/20 (January–May 2020).**

208

209 Figure 1 presents the amplitude of DW1 after low-pass filtering and the zonal wind observed by the Singapore sonde. Only
 210 amplitude components with periods longer than 13 months are retained. In the stratosphere, the zonal wind shows alternating
 211 downward propagating westerly wind (positive value in Figure 1e and 1f) and easterly wind (negative value in Figure 1e and

212 1f). Each westerly and easterly transition can be called a QBO cycle. In the stratosphere (Figure 1c and 1d), below 40 km, the
 213 amplitude of DW1 also shows Quasi-Biennial variability. Above 40 km, the variation becomes more complex. This feature
 214 will be discussed later. In the MLT region (Figure 1a and 1b), the low-pass filtering results of DW1 at the equator exhibit
 215 Quasi-Biennial variability, with amplitude peaks observed around 90 and 100 km. Comparing the DW1 amplitudes in MLT
 216 with the zonal wind, the result reveals that the variations in DW1 amplitude correspond to the zonal wind between 20 and 30
 217 hPa. The amplitude of DW1 is stronger during the QBO westerly wind phase than during the QBO easterly wind phase. This
 218 result is consistent with Garcia (2023) that the wind fields of QBO at altitudes below 27 km are clearly correlated with the
 219 DW1 amplitude. Accordingly, in this work, the zonal wind between 20 and 30 hPa is used as the criterion for defining the
 220 QBO for DW1.

221 During February–May 2016 and January–May 2020, two QBO disruption events occurred (Wang et al., 2023). As shown in
 222 Figure 1f, the phenomenon ranges from 40 to 15 hPa in 2016 and from 40 to 20 hPa in 2020, which is consistent with previous
 223 work (Anstey et al., 2021; Newman et al., 2016). Notably, the disruption region coincides with the QBO criterion altitude for
 224 DW1. To evaluate how the DW1 exhibits responses to the events, the corresponding time intervals are highlighted with vertical
 225 green dashed lines. In the stratosphere (Figure 1d), within the disruption periods, amplitude enhancements are observed below
 226 40 km compared to other QBO easterly phases. Similarly, in the MLT region, the DW1 amplitudes show responses to these
 227 events (Figure 1b). As shown in Figures 1a and 1b, DW1 amplitudes above 70 km are stronger during these disruption events
 228 than during other QBO easterly phases, though they remain weaker than those observed during the QBO westerly phase. This
 229 enhancement is particularly evident around 90 and 100 km.

230 SD-WACCM-X simulations reproduce the SABER observations of DW1 remarkably well in response to QBO disruptions. In
 231 Figures 1a, 1b, 1f, and 1g, both datasets show enhanced amplitudes during the February–May 2016 and January–May 2020
 232 events. The difference arises in vertical structure and magnitude. Above 70 km, SABER exhibits three distinct DW1 peaks
 233 near 80, 90, and 100 km, whereas SD-WACCM-X shows a single peak at approximately 108 km. In the stratosphere above
 234 40 km, both model and observations peak at similar altitudes, but the simulated amplitudes remain weaker than SABER result.
 235 Below 40 km, the model captures the QBO-modulated DW1 seen in Figures 1c, 1d, 1i, and 1j. These discrepancies likely stem
 236 from the MERRA-2 nudging applied up to ~50 km in SD-WACCM-X. In this nudged region, DW1 comprises both propagating
 237 and non-propagating components (Garcia, 2023; Chapman & Lindzen, 1970). Sakazaki et al. (2018) showed that MERRA-2
 238 may underestimate the contribution of the non-propagation mode of DW1 (Figure 4 in that work). This feature may explain
 239 why the amplitude of DW1 is lower than that in SABER and the complex variation of SABER above 40 km.

240 To assess the DW1 response to QBO disruption events over a broad latitude range, the differences between QBO disruption
 241 and regular QBO easterly and westerly phases are calculated. The DW1 amplitudes used are the result after 13 months low-
 242 pass filtering. Since the DW1 amplitudes typically peak between February and April each year (e.g., Xu et al., 2009; Mukhtarov
 243 et al., 2009; Garcia, 2023), only the amplitudes during these three months are considered. The classification method for
 244 different QBO phases is as follows. Regular QBO phases were classified using the following method. QBO westerly phase
 245 (QBOW): February–April zonal wind at 20 hPa is continuously westerly, or zonal wind at 30 hPa is westerly while 20 hPa

undergoes an easterly-to-westerly transition. Easterly phase (QBOE): any remaining cases. The selection of regular QBO phases is limited to data from 2002 to 2014, as QBO disruption events occurred after 2015. Additionally, since observations in 2002 are mainly available from March to April, data from this year are excluded. The years 2004, 2006, 2008, 2011, 2013, and 2014 are classified as QBOW; 2003, 2005, 2007, 2009, 2010, and 2012 as QBOE. For each phase, all filtered amplitudes across the selected months are averaged, while processing data for 2016 and 2020 separately. This approach enables a direct comparison of DW1 amplitude anomalies in both latitude and altitude between disruption and regular QBO conditions.

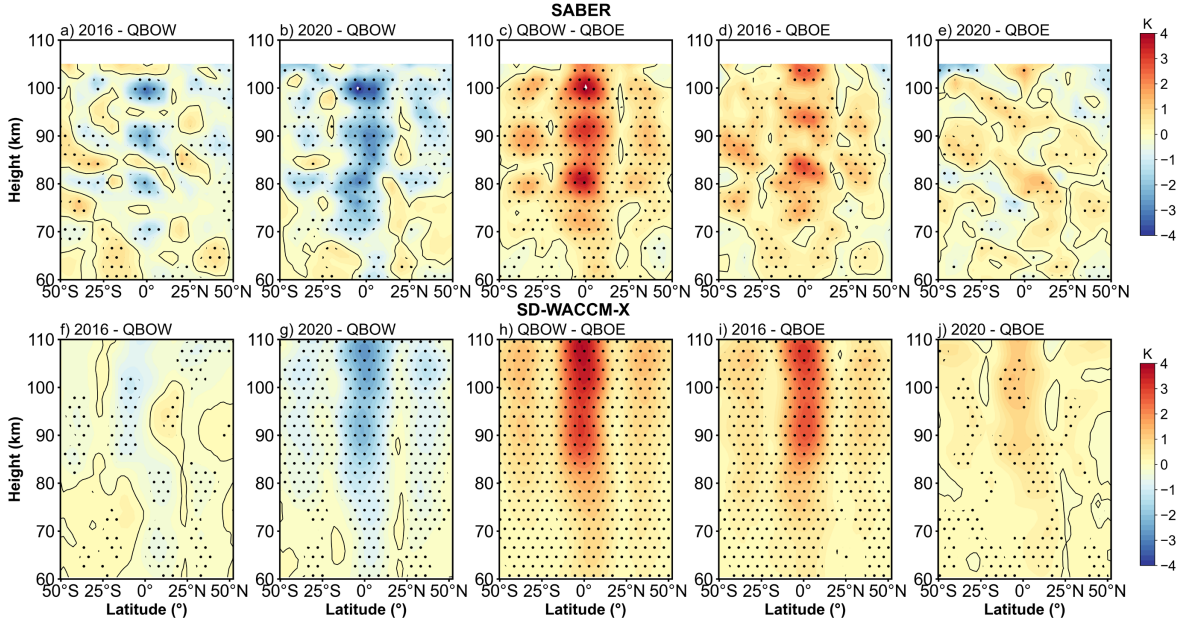
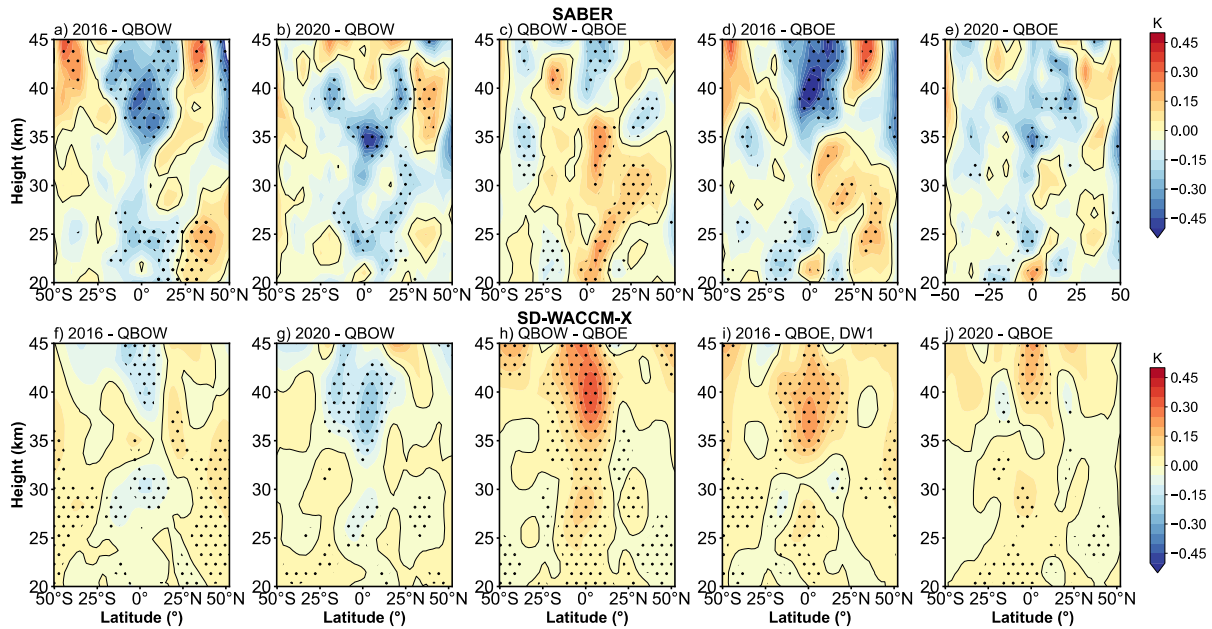


Figure 2. Amplitude differences of the DW1 after low-pass filtering between different QBO phases in the mesosphere and lower thermosphere (MLT) as a function of latitude and altitude. The difference is based on the average from February to April. (a-e) are corresponding to the difference from the 2016 disruption event minus QBO westerly phases (2016-QBOW), 2020 disruption event minus QBO westerly (2020-QBOW), QBO westerly minus QBO easterly (QBOW-QBOE), 2016 disruption event minus QBO easterly (2016-QBOE) and 2020 disruption event minus QBO easterly (2020-QBOE). (f-j) is similar to (a-e) but for SD-WACCM-X simulation result. The black lines indicate the zero lines. The dotted areas indicate the differences that are significant at the 95% confidence level.

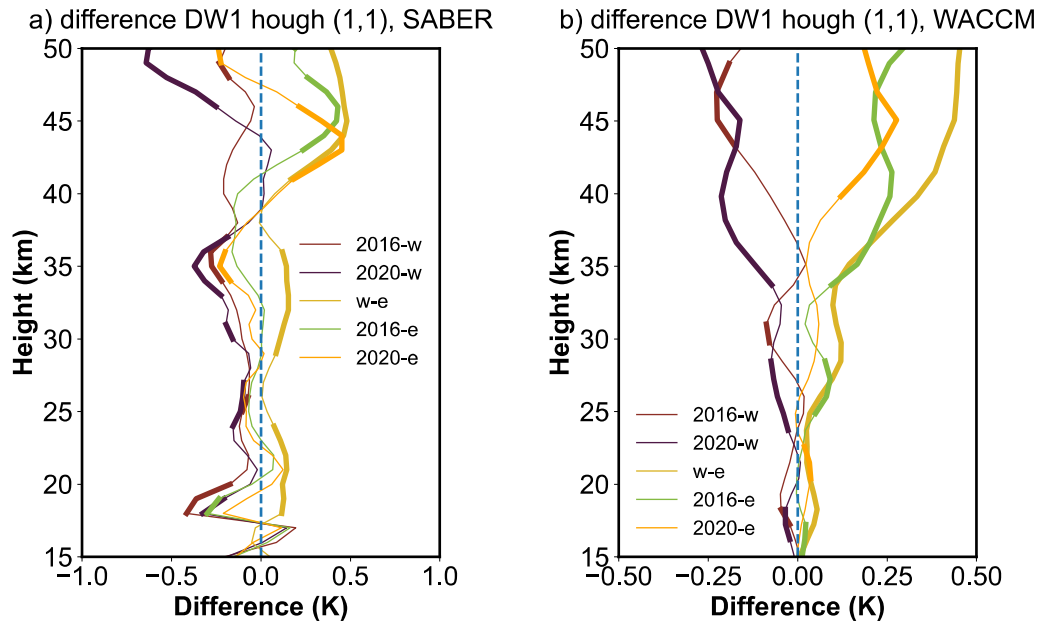
Figure 2 gives the difference in DW1 amplitudes during various QBO phases in the MLT region. The significance of the differences was assessed using Welch's t-test, and values exceeding the 95 % confidence threshold are highlighted in dotted. The five columns correspond to the 2016 disruption event minus QBO westerly (2016-QBOW), 2020 disruption event minus QBO westerly (2020-QBOW), QBO westerly minus QBO easterly (QBOW-QBOE), 2016 disruption event minus QBO easterly (2016-QBOE) and 2020 disruption event minus QBO easterly (2020-QBOE), respectively. The relative change

267 between different QBO phases is also calculated (e.g., $\frac{QBOW-QBOE}{QBOE}$, and so on). The comparison between QBOW and QBOE
 268 (Figure 2c) reveals that DW1 amplitudes are significantly larger during QBOW, particularly at the equator and around 30°N/S
 269 above ~75 km. The enhancements reach ~2.79 K (~34.5 %) at the equator and ~0.79 K (~20.6 %) at 30°N/S, with peak values
 270 as high as ~3.30 K (~38.5 %) and ~1.19 K (~31.7 %) at respective latitudes. During the 2016 disruption (Figures 2a, 2d), DW1
 271 amplitudes lie between QBOE and QBOW values. The clear enhancement could be found from 75 km to 105 km. The pattern
 272 in 2016–QBOE closely resembles that of QBOW–QBOE, although the equatorial peaks appear at slightly higher altitudes.
 273 The enhancements reach ~1.56 K (~20.5 %) at the equator and ~0.54 K (~14.4 %) at 30°N/S. The peak enhancements relative
 274 to QBOE reach ~2.40 K (~26.5 %) at the equator and ~0.87 K (~29.5 %) at 30°N/S. Compared to QBOW, however, the
 275 difference drops to -2.28 K (-18.8 %) at equator and ~0.12 K (4.6 %) at 30°N/S. In contrast, the 2020 disruption event shows
 276 weaker amplitude increases relative to QBOE (Figures 2b, 2e). The clear enhancement occurs from 75 km to 90 km. The
 277 increment reaches ~0.50 K (~6.0 %) at the equator and ~0.26 K (~7.7 %) at 30°N/S, with a peak enhancement of only ~0.91
 278 K (~11.6 %) at the equator and ~0.31 K (~14.2 %) at 30°N/S. Compared to QBOW, the difference is -2.3 K (~-21.1%) at the
 279 equator and -0.57 K (~-12.0 %) at 30°N/S. These values are considerably lower than those observed during the 2016 event or
 280 the typical QBOW enhancement. The SD-WACCM-X model reproduces the general features described above (Figures 2f–2j),
 281 though the vertical structure of the simulated amplitudes differs slightly from observations.



283
 284 **Figure 3. Similar to figure 2 but in stratosphere. (a-e) give the difference result derived from SABER. (f-g) give the difference result**
 285 **derived from SD-WACCM-X.**
 286

287 Figure 3 compares the stratospheric DW1 amplitude differences derived from the SABER dataset and SD-WACCM-X
 288 simulations. The enhancement pattern resembles that seen in the MLT region but is confined to tropical latitudes. Because
 289 SABER exhibits complex variability above 40 km, the analysis is restricted to altitudes below that level. As shown in Figure
 290 3c, the DW1 amplitudes during QBOW exceed those during QBOE by ~ 0.21 K ($\sim 37.9\%$) at around 20–25 and 30–35 km.
 291 In SD-WACCM-X result (Figure 3h), the positive peaks are found at 25–30 km and 35–40 km, which is ~ 0.21 K ($\sim 27.4\%$).
 292 The amplitudes during the disruption events are much weaker relative to those during QBOW phases shown in both datasets
 293 (Figure 3a, 3b, 3f and 3g). Compared to QBOE, the strengthening during the 2016 QBO disruption event occurs at
 294 approximately 30–35 km in SABER (Figure 3d) and 35–45 km in SD-WACCM-X (Figure 3i), which is ~ 0.15 K ($\sim 21.8\%$)
 295 and 0.20 K ($\sim 23.9\%$), respectively. During the 2020 event, the amplitudes are comparable to those during QBOE (Figure 3e
 296 and 3j).



297
 298 **Figure 4. Amplitude differences profiles of the DW1 (1, 1) mode after low-pass filtering between different QBO phases in the**
 299 **stratosphere like Figure 2. (a) gives the difference result derived from SABER. (b) give the difference result derived from SD-**
 300 **WACCM-X. The bold lines indicate the differences that are significant at the 95% confidence level.**

301
 302 Figure C2 presents the low-pass time series of the equatorial DW1 amplitude and the (1,1) mode amplitude at 95 km, showing
 303 that the (1,1) mode closely follows the equatorial DW1 amplitude. In the stratosphere, however, the superposition of
 304 propagating tides and trapped modes complicates the interpretation. To separate these contributions, Figure C1 compares the
 305 amplitudes of the (1,1) and (1, -2) modes under different QBO phases. The trapped mode is dominant below 60 km, while the
 306 (1,1) mode is relatively weaker. A clear distinction between QBOW and QBOE is evident in the (1,1) mode (Fig. C1a), whereas
 307 the (1, -2) mode shows little difference between the phases. Together, Figures C1 and C2 indicate that the (1,1) mode captures

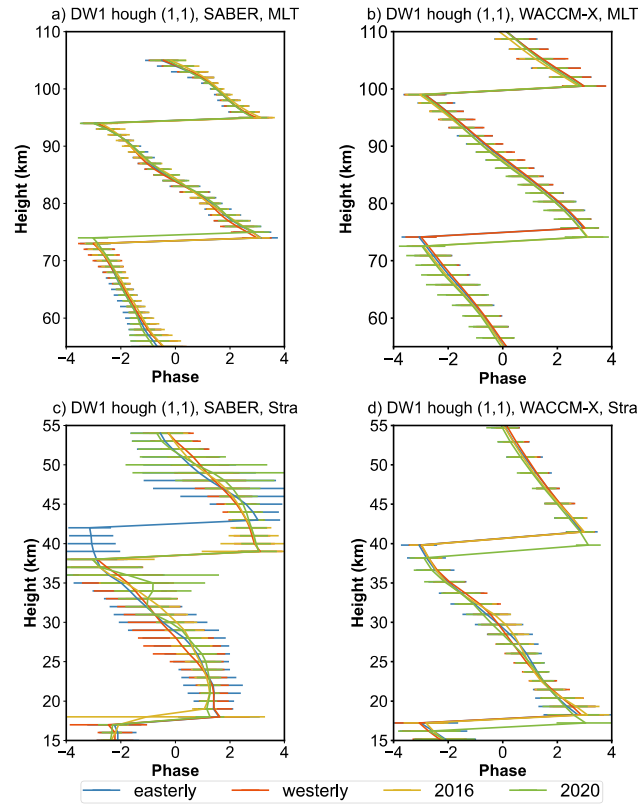
308 nearly all of the QBO-related variability in the MLT region, motivating a closer examination of the (1,1) mode in the
309 stratosphere.

310 Figure 4 shows the vertical profiles of amplitude differences in the DW1 (1,1) mode between QBO phases after low-pass
311 filtering. The bold lines denote differences significant at the 95% confidence level. In SABER observations (Fig. 4a),
312 amplitudes during QBOW exceed those in QBOE throughout 20–45 km. During the 2016 and 2020 events, amplitudes remain
313 close to those in QBOE between 20–40 km but become stronger above 40 km, with maximum differences of ~ 0.15 ($\sim 11\%$),
314 -0.18 ($\sim 12\%$), ~ 0.36 K ($\sim 36\%$), ~ 0.21 K ($\sim 21\%$), and ~ 0.18 K ($\sim 17\%$) for 2016-QBOW, 2020-QBOW, QBOW-QBOE,
315 2016 - QBOE, and 2020-QBOE, respectively. WACCM-X simulations (Fig. 4b) reproduce a similar vertical pattern: during
316 the disruption events, amplitudes lie between QBOE and QBOW values in the 20–50 km region.

317 **3.2 DW1 phases response to QBO disruption events**

318 In this section, whether the DW1 phases and wavelengths respond to QBO disruptions will be analysed. As discussed above,
319 the DW1 QBO variability is mainly in (1, 1) mode. Hence, we focus on the phase of (1, 1) mode. As noted previously, the
320 pronounced DW1 amplitude observed from February to April renders the phase during this period an important variable. Hence,
321 the statistics are based on these periods. Since the phase values change cyclically (e.g., it jumps from π to $-\pi$), causing the
322 overestimation of the standard deviation. We apply the following method. We first calculate averages and standard deviation
323 (or error) of sine and cosine Fourier components, and then calculate the average phase and its confidence interval using error
324 propagation. The mean value and its 95% confidence interval in different QBO phases (listed in section 3.1) are calculated.
325 The statistical results for the phases in 2016 and 2020 are calculated separately.

326



327

328 **Figure 5. The DW1 (1, 1) mode vertical phase structure in mesosphere and lower thermosphere (MLT) and stratosphere averaged**
 329 **from February to April during QBO westerly phase (orange), QBO easterly phase (blue), 2016 QBO disruption event (yellow) and**
 330 **2020 QBO disruption event (green). (a, c) give the SABER observation result. (b, d) give the WACCM-X simulations. The error bar**
 331 **denotes the 95% confidence interval of the phases for each height.**

332

333 Figure 5 illustrates the vertical phase structure of DW1 (1, 1) mode in the mesosphere and lower thermosphere (MLT) and
 334 stratospheric regions, respectively, averaged over the February–April period. The results are presented for various QBO phases
 335 at different latitudes, based on data from (a, c) SABER and (b, d) SD-WACCM-X. Error bars indicate the 95% confidence
 336 interval of the phase average. The lines represent different QBO phases and events: QBO westerly phase (orange), QBO
 337 easterly phase (blue), the 2016 QBO disruption event (yellow), and the 2020 QBO disruption event (green).

338 In the MLT region (Figure 5a and 5b), the vertical phase profiles exhibit minimal differences across the QBO westerly, easterly
 339 and 2016 phases. The structures are nearly identical in both the simulations and observations, with two phase peaks
 340 (approximately π rad) consistently present. The peak altitudes remain almost unchanged among the different QBO phases,
 341 suggesting a limited phase response to QBO disruption events in the MLT region. During the 2020 event, the phase peaks at
 342 around 75 km is higher than that during other QBO phases in SABER and lower than that in WACCM-X.

343 The DW1 vertical phase structures in the stratosphere region are given in Figure 5c and 5d. In SABER observations, there are
 344 clear differences between QBOW and QBOE. The phase peaks (at around 40 km) during the QBOW occur about 3 km lower
 345 than those during QBOE. During the QBO disruption events, the phase structure is similar to that during the QBOW. From
 346 WACCM-X simulations, the feature is similar to the pattern in MLT (Figure 5b). During the 2020 disruption event, the phase
 347 peaks are lower than other QBO phases by about 1 km.
 348 The phase peaks described above ($\sim\pi$ rad) are used to calculate the DW1 wavelengths in both the stratosphere and MLT regions.
 349 The altitude difference between the two peaks is taken as the wavelength, following the method of Liu et al. (2021). The
 350 statistical results of DW1 (1, 1) mode wavelengths under different QBO phases are summarized in Table 1, which lists the
 351 mean values and standard deviations at various altitudes. In the MLT region, the mean wavelengths are ~ 21 km in the SABER
 352 dataset and ~ 25 km in the SD-WACCM-X dataset. The wavelengths during QBO disruption events are comparable to those
 353 during the QBO westerly and easterly phases, a feature also captured in the SD-WACCM-X simulations. In the mesosphere,
 354 the mean wavelengths are ~ 34 km in SD-WACCM-X and ~ 33 km in SABER. In this region, there are clear differences between
 355 QBOW and QBOE. The QBOE wavelength is about 2 km shorter than that during QBOW. In the stratosphere, the QBOE
 356 wavelength is about 2 km longer than that during QBOW. The wavelengths during the QBO disruptions are close to those
 357 during QBOW.
 358 According to the theoretical framework proposed by Forbes and Vincent (1989) and Kogure and Liu (2021), zonal winds
 359 modify the intrinsic frequency of tides through Doppler shifting, thereby altering their vertical wavelengths. Specifically,
 360 westerly winds lead to longer DW1 vertical wavelengths, whereas easterly winds result in shorter ones. However, the
 361 dependence shown in Table 1 differs from that reported in previous studies. This discrepancy can be attributed to differences
 362 in methodology. In this study, the vertical wavelengths are determined from the phase difference between adjacent peaks ($+\pi$).
 363 In the stratosphere, one of these peaks typically occurs in the lower stratosphere (~ 18 km) and the other in the upper
 364 stratosphere (~ 40 km). Consequently, the estimated wavelengths encompass the combined influences of both the QBO and
 365 SAO, producing a mixed result that deviates from earlier findings.

366
 367 **Table 1. The comparison of mean (left of the slash) and standard deviations (right of the slash) of DW1 (1, 1) mode wavelengths (in**
 368 **km) revealed by SD-WACCM-X and SABER from 15 km to 105 km between QBO westerly phase, easterly phase, 2016 disruption**
 369 **event and 2020 disruption event calculated from February to April.**

Data	SD-WACCM-X			SABER		
altitude	~ 15 km – ~ 40 km	~ 40 km – ~ 75 km	~ 75 km – ~ 105 km	~ 15 km – ~ 40 km	~ 40 km – ~ 75 km	~ 75 km – ~ 105 km
Westerly	22.97/1.49	34.47/1.79	25.10/1.84	21.81/1.44	33.12/1.78	21.29/1.04
Easterly	22.51/1.73	34.42/2.15	25.60/2.20	24.46/1.99	30.84/2.35	20.56/1.30

2016	22.56/1/33	33.26/1.58	25.58/2.03	21.48/2.31	33.32/2.10	21.28/0.85
2020	22.71/1.87	33.80/2.68	26.27/2.41	21.08/1.77	34.24/1.46	20.39/1.35

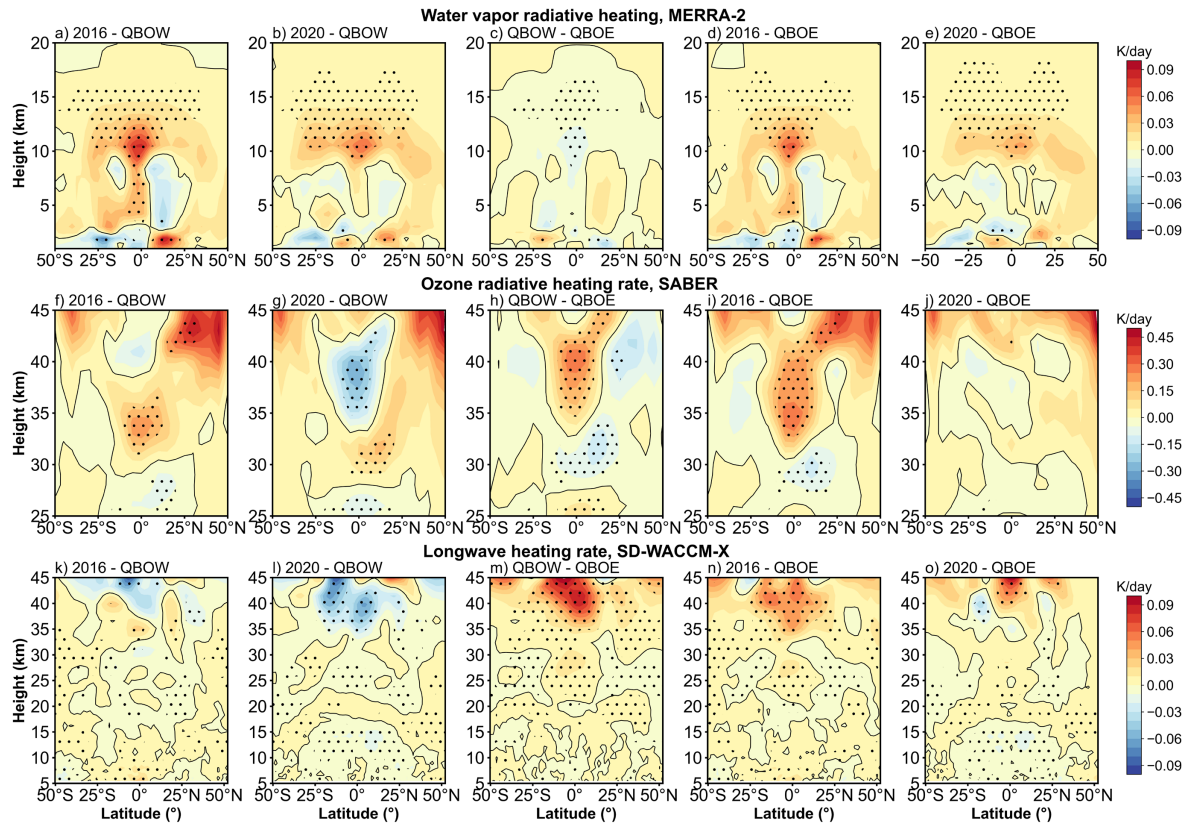
370

371 4 Discussion

372 In this section, we discuss how the QBO disruptions modulate the DW1 by several mechanisms from the lower atmosphere to
373 the upper atmosphere. As in Introduction, three primary mechanisms are considered: background zonal wind and its latitudinal
374 shear (e.g., Forbes and Vincent, 1989; Hagan et al., 1999; McLandress, 2002b); diurnal heating (McLandress, 2002b; Riggins
375 and Lieberman, 2013; Ortland, 2017); tide–gravity wave (GW) interactions (Mayr et al., 1998; McLandress, 2002a; Lu et al.,
376 2012; Wang et al., 2024). The mechanism analysis will be organized by tidal heating (troposphere and stratosphere), the
377 dissipation and tidal propagation (from stratosphere to mesosphere) and tide-gravity wave interaction (mesosphere and lower
378 thermosphere).

379 4.1 Tidal heating variation during the QBO disruption events

380 The excitation sources of DW1 can be broadly classified into three categories: (1) solar radiation in the near-infrared (IR)
381 absorbed by tropospheric H₂O, (2) solar radiation in the ultraviolet (UV) absorbed by stratospheric and lower mesospheric O₃,
382 and (3) solar radiation absorbed by O₂ in the Schumann–Runge bands and continuum (Hagan, 1996). Additionally, Kogure
383 and Liu (2021) highlighted the role of latent heating in modulating DW1. It is worth noting that the timing of the 2016 QBO
384 disruption event coincides with the phase of the extreme El Niño (e.g., Santoso et al., 2017; Hu and Fedorov, 2017). El Niño
385 itself could modulate the DW1 (Kogure and Liu, 2021). Attention should be paid to the contribution of water vapor and latent
386 heating jointly influenced by QBO disruption and 2015/16 extreme El Niño. Overall, this section focuses on examining the
387 effects of water vapor radiative heating, ozone radiative heating, and latent heating on DW1.



388

389 **Figure 6. As in Figure 2 and Figure 3, but the difference of amplitude in DW1 component (after low-filtering) of (a-e) water vapor**
 390 **heating rate DW1 component from MERRA-2, (f-j) ozone heating rate DW1 component from SABER and (k-o) longwave heating**
 391 **rate from SD-WACCM-X. The dotted areas indicate the differences that are significant at the 95% confidence level.**

392

393 Figure 6 presents the difference of amplitude in the DW1 component of water vapor radiative heating rate, ozone radiative
 394 heating rate, and longwave heating rate. The calculation method is consistent with the method described in Section 3.1. During
 395 QBOE and QBOW, the DW1 component of water vapor heating remains nearly unchanged (Figure 6c). However, during the
 396 2016 QBO disruption (Figures 6a, 6d), a notable enhancement in water vapor heating appears between 10–13 km altitude
 397 around the equator. The difference between 2016 and QBOE is $\sim 0.02 \text{ K day}^{-1}$ with increases of $\sim 2.5\%$ relative to QBOW. The
 398 difference between 2016 and QBOW is 0.03 K day^{-1} with increases of $\sim 3.7\%$ relative to QBOW. A similar pattern is seen
 399 during the 2020 QBO disruption event (Figures 6b and 6e). The relative changes of the regional average increase by $\sim 1.2 \%$
 400 compared to QBOW and $\sim 2.3 \%$ compared to QBOE.

401 Figures 6f–6j reveal that the largest QBO-related differences in the DW1 component of ozone heating occur near the equator
 402 between 30 and 45 km. In QBOW, ozone heating rates between 35 and 45 km exceed those in QBOE by $\sim 2.1 \%$ (Figure 6h).
 403 During the 2016 QBO disruption event (Figures 6f and 6i), ozone radiative heating rates are $\sim 3.6 \%$ larger than those in the

404 QBOW between 30 and 35 km and $\sim 2.9\%$ larger than those in the QBOE within the 30–40 km range. In contrast, during the
 405 2020 disruption event (Figures 6g and 6j), the ozone heating rate is comparable to that of the easterly phase and lower than
 406 that of the westerly phase in the 35–45 km altitude range.

407 In the SD-WACCM-X simulation, the longwave heating rate accounts for the effects of three major absorbers: H_2O , CO_2 , and
 408 O_3 (Neale et al., 2010). This parameter could be used to verify the effect of the water vapor and ozone radiative heating. The
 409 DW1 component of the longwave heating rate from SD-WACCM-X is shown in Figures 6k–6o. The heating rate difference
 410 between the QBOW and QBOE reveals a positive peak at 40 km near the equator, with no significant difference at the
 411 equatorial tropopause (Figure 6m). The feature corresponds to the observed pattern (Figures 6c and 6h). In the 2016 disruption
 412 case, the simulated equatorial heating rate exhibits positive peaks around 35 km and 15 km (not significant), aligning well with
 413 observations in terms of altitude (Figure 6k and 6n). In the 2020 disruption case, the simulation (Figure 6l and 6o) agrees with
 414 the observed stratospheric heating features (Figures 6g and 6j). However, at around 15 km, the simulation shows negative
 415 peaks near the tropopause, whereas the observations indicate positive peaks (Figures 6b and 6e). As longwave heating
 416 incorporates contributions from multiple absorbers, the discrepancies may be attributed to the influence of other constituents.

417 As discussed above, the (1,1) Hough mode captures nearly all QBO-related variability in the MLT. Accordingly, the (1,1)
 418 component of the ozone heating rate is extracted for diagnosis. Numerous studies have noted that the vertical thickness of
 419 ozone heating (~ 40 km) is large compared with the relatively short vertical wavelength of the DW1, implying weak projection
 420 onto the (1,1) and thus limited excitation efficiency (e.g., Chapman and Lindzen, 1970; Hagan, 1999; Garcia, 2023). Studies
 421 with GSWM and the Tide Mean Assimilation Technique (TAMT) further indicate that DW1 forced by ozone heating tends to
 422 be out of phase with DW1 forced by water-vapor heating, reducing the amplitudes (Hagan, 1996; Ortland et al., 2017).
 423 Consistent with this mechanism, MLS observations show a pronounced depression of the tropical diurnal tide near 1.0 hPa
 424 (~ 49.5 km; Wu et al., 1998), which may be attributed to interference between the upward-propagating (1,1) tide and a locally
 425 forced component from ozone heating. Figure 7 compares DW1 (1,1) temperature and ozone heating rate between different
 426 QBO phases and shows a suppressed (1,1) amplitudes feature around ~ 50 km, while ozone heating peaks slightly below this
 427 level. This feature aligns with the MLS evidence. Therefore, the ozone may not play a positive role for the DW1 (1, 1) mode.
 428 Whether ozone heating modulated DW1 (1, 1) mode requires more detailed investigation like model simulation from Kogure
 429 et al. (2023).

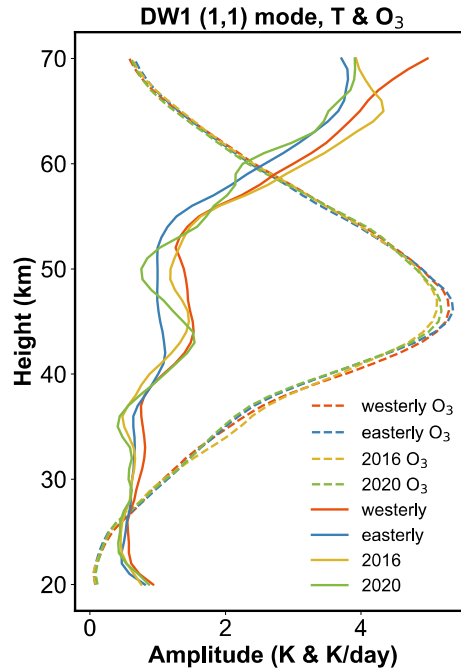
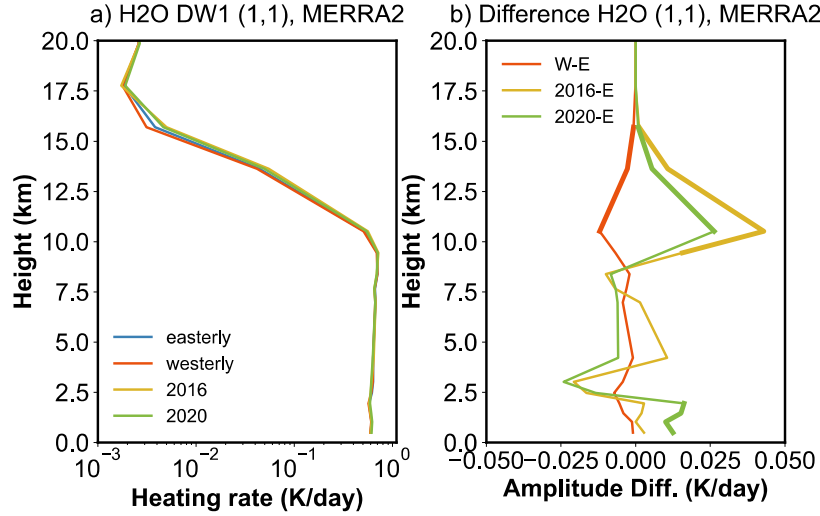


Figure 7. The comparison between the temperature and heating rate of the DW1 (1, 1) mode between different QBO phases.

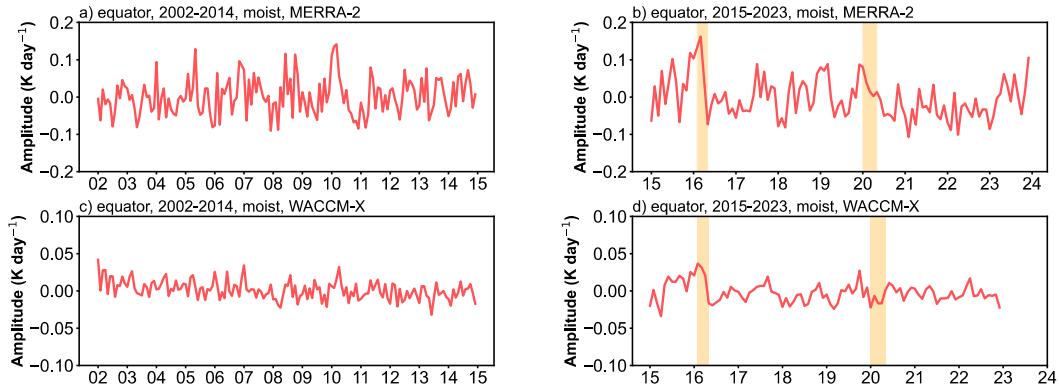
The DW1 (1,1) mode is primarily excited by water-vapor heating (Forbes and Garrett, 1978). As shown in equation A1 and A10 in Appendix A, the concentration of water vapor is one of the key factors controlling water vapor radiation. During the 2016 QBO disruption, which coincided with the strong 2015/2016 El Niño, the two phenomena jointly modulated the DW1 water vapor heating sources. El Niño enhances moisture anomalies that increase with altitude, culminating in pronounced positive signals in the upper troposphere and lower stratosphere (UTLS) (Johnston et al., 2022). In contrast, the occurrence of the 2016 QBO disruption introduces a shear transition from westerly to easterly near 40 hPa, which strengthens tropical upwelling and lowers cold-point temperatures. This dynamical response injects H₂O-poor air into the lower stratosphere, partially offsetting the El Niño-driven moistening. The water vapor concentrations remain above the climatological seasonal cycle under the modulation of these two phenomena (Diallo et al., 2018). Unlike 2016, the 2020 disruption produces only weak lower-stratospheric dehydration (~2–3 %) because enhanced upwelling and cold-point cooling are suppressed. Instead, anomalously warm tropopause temperatures associated with Australian wildfire smoke facilitate significant moistening of the lower stratosphere (Diallo et al., 2022). It is foreseeable that the increase in water vapor concentration modulated by QBO disruptions and 2015/16 El Niño event will lead to an increase in the radiative heating rate of water vapor.

Figure 8 presents the water vapor radiative heating rate profiles of the DW1 (1,1) mode for different QBO phases and their differences. The heating rate exhibits large values in the troposphere, extending up to ~10 km. The average magnitude could reach ~0.62 K day⁻¹. During the 2016 QBO disruption event (Fig. 8b), the maximum difference occurs at 10.5 km, reaching 0.043 K day⁻¹, which represents an ~8 % increase relative to QBOE. However, the DW1 amplitude varies by ~20.5 % compared

450 to QBOE, indicating that water-vapor heating accounts for only $\sim 39\%$ of the observed amplitude difference. This feature
 451 suggests that additional mechanisms must be involved. A similar enhancement of water-vapor heating is observed during the
 452 2020 event, with the largest difference again at 10.5 km ($\sim 0.026 \text{ K day}^{-1}$), corresponding to an $\sim 5\%$ increase relative to QBOE.
 453



454
 455 **Figure 8. Heating rate profiles of the DW1 (1, 1) mode between different QBO phases and their differences. (a, b) give the water**
 456 **vapor heating profile and its difference derived from MERRA2. The bold lines indicate the differences that are significant at the**
 457 **95% confidence level.**
 458



459
 460 **Figure 9. (a, b) The deseasonalized time series of DW1 amplitudes of latent heating rate (K day^{-1}) at equator averaged from 800 hPa**
 461 **to 200 hPa derived from MERRA-2. (c-d) is as in (a-b) but from SD-WACCM-X. The orange-filled areas represent two QBO**
 462 **disruption events.**

463 Figure 9 shows the deseasonalized time series of the DW1 component of latent heating rate (K day^{-1}) at the equator, averaged
 464 from 800 hPa to 200 hPa. In this tropospheric layer, the latent-heating signal shows less differences between QBOW and
 465 QBOE phases. Therefore, deseasonalization is directly applied to the full time series without separating the two QBO states.

466 In MERRA-2 and SD-WACCM-X, the anomaly peaks reach 0.162 K day^{-1} and 0.037 K day^{-1} , respectively, which correspond
 467 to increases of about $\sim 32 \%$ and $\sim 25 \%$ above their climatological means (0.50 K day^{-1} and 0.15 K day^{-1}). When averaged
 468 over February-April in 2016, the anomalies remain elevated at 0.11 K day^{-1} ($\sim 22 \%$) in MERRA-2 and 0.03 K day^{-1} ($\sim 19.2 \%$)
 469 in SD-WACCM-X. In contrast, during the 2020 QBO disruption event, the amplitudes in both MERRA-2 and SD-WACCM-
 470 X remain closer to the climatological means, with deviations of 0.018 K day^{-1} and $-0.013 \text{ K day}^{-1}$, respectively. These results
 471 suggest that latent heating may contribute to the amplification of DW1 amplitudes during the 2016 QBO disruption event but
 472 show little effect during the 2020 event.

473 **4.2 Effect of zonal wind and its latitude shear during the events**

474 In this section, we focus on the effects of the background wind on tides during their upward propagation. As discussed in
 475 Forbes and Vincent (1989), zonal winds distort the tidal expansion functions such that they are amplified and broadened in the
 476 winter hemisphere ($U > 0$) but are considerably diminished under summer conditions. As shown in Figure 1f, during the 2016
 477 QBO disruption, the westerly wind layer is unusually thick in the stratosphere, though still weaker than in the normal QBO.
 478 In contrast, during the 2020 event, the westerly wind layer is extremely shallow, essentially indistinguishable from the easterly
 479 phase. Thus, the zonal wind in the stratosphere during the 2016 QBO disruption is conducive to the growth of tidal amplitude.
 480 During the 2020 QBO disruption event, the influence of zonal winds in the stratosphere on tides is essentially consistent with
 481 that observed during the QBOE period.

482 Additionally, the zonal wind influences the intrinsic frequency through Doppler shifting and therefore modifies the variation
 483 of the vertical wavenumber. The increase or decrease of the vertical wavenumber depends on the direction of zonal wind.
 484 Under the usual Newton-cooling/Rayleigh-friction parameterizations, the effective dissipation is approximately proportional
 485 to the squared local vertical wavenumber (Forbes and Vincent, 1989; Kogure and Liu, 2021). Consequently, zonal wind could
 486 also influence the dissipation process. To examine the dissipation during the event, we apply the amplitude ratio method.

487 As in Forbes and Vincent (1989), the amplitude growth equation is:

$$488 \quad \frac{A(z)}{A(70)} = \exp \left\{ \int_{70}^z \left[-k_i + \frac{1}{2H} \right] dz \right\} \quad (3)$$

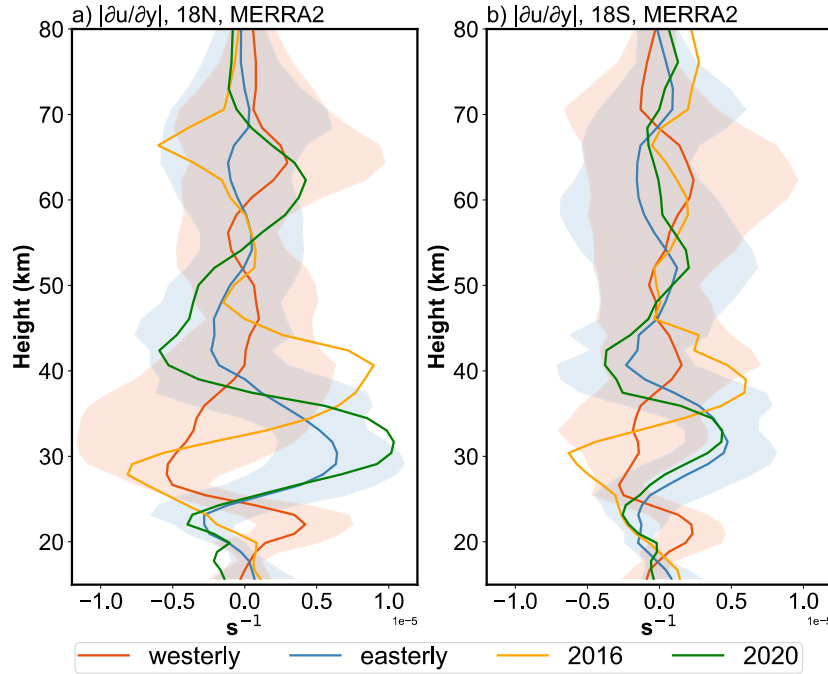
489 where A is the amplitude, z is the altitude (in km), H is the local scale height and k_i is the imaginary part of the complex
 490 vertical wavenumber that governs the damping of the amplitude profile. Calculating the ratio of amplitude using Equation (3)
 491 during two different QBO phases (e.g., 2016/QBOE) yields:

$$492 \quad \frac{A_{2016}(z)}{A_{QBOE}(z)} = \exp \left\{ \int_{70}^z - \left(k_{i,2016}(z) - k_{i,QBOE}(z) \right) dz \right\} \quad (4)$$

493 The scale height term is removed, leaving the dissipation term. Thus, the changes in amplitude ratio may reflect tidal dissipation
 494 variations at the altitude.

495 Figure C3 presents the ratio results derived from SABER observations and SD-WACCM-X simulations. In the SABER data
 496 (Figure C3a), during the 2016 event, two distinct peaks appear in the lower stratosphere near 22 km and 30 km when comparing
 497 the disruption events with the QBOE phase (green lines), possibly indicating relatively less dissipation during the 2016 QBO

498 disruptions. During the 2020 event, the lower peak (~ 22 km) is close to that during 2016 event, while the upper peak (~ 30 km)
 499 is relative weak to the 2016 event. This may suggest a relatively large dissipation at those heights. The SD-WACCM-X
 500 simulations reproduce a similar pattern, although the peak altitudes differ slightly. All simulated ratios remain above 1, which
 501 may indicate stronger tidal source activity in the SD-WACCM-X simulations. Overall, these results suggest that during QBO
 502 disruptions, zonal wind may lead to relatively less dissipation processes, thereby affecting DW1 amplitudes.
 503 In addition to zonal-mean wind effects, latitudinal shear of zonal wind in the subtropical mesosphere can modulate the seasonal
 504 variability of the (1,1) mode (McLandress, 2002b; Mayr and Mengel, 2005; Sakazaki et al., 2013; Kogure et al., 2021; Siddiqui
 505 et al., 2022). Large values of $|\partial u/\partial y|$ at some heights are equivalent in some sense to faster rotation, which restricts the
 506 latitudinal band or waveguide where the diurnal tide can propagate vertically, thus reducing the tidal amplitude above by
 507 removing tidal energy at that altitude (McLandress, 2002b; Siddiqui et al., 2022). The wind shear at 18°N/S is a typical
 508 indicator (Kogure et al., 2021).



509
 510 **Figure 10. The $|\partial u/\partial y|$ profiles after deseasonalized between different QBO phases at (a) 18°N and (b) 18°S . The colourful shaded**
 511 **areas denote one standard deviation of the phases for each height.**

512
 513 The monthly $|\partial u/\partial y|$ at 18°N/S is calculated, deseasonalized, and classified following the method described in Section 3.1. The
 514 $|\partial u/\partial y|$ profiles for different QBO phases are shown in Figure 10. During QBOW, a pronounced negative anomaly appears
 515 near 30 km, whereas during QBOE a strong positive anomaly is evident at the same altitude. During the 2016 disruption event,
 516 the $|\partial u/\partial y|$ profile at 18°N exhibits a structure broadly similar to that of QBOW. However, from 35 to 45 km it shows strong
 517 positive values, a feature not observed in other QBO phases. The $|\partial u/\partial y|$ profile at 18°S displays a similar vertical structure

518 but with smaller amplitudes. Based on this structure, the tide may be amplified near 30 km and subsequently damped near 40
 519 km, which could partly explain why the tidal amplitudes during the 2016 disruption do not reach those observed in QBOW. In
 520 contrast, the $|\partial u / \partial y|$ during the 2020 disruption event closely resembles the QBOE structure, suggesting that the tidal
 521 propagation background was similar to QBOE conditions.

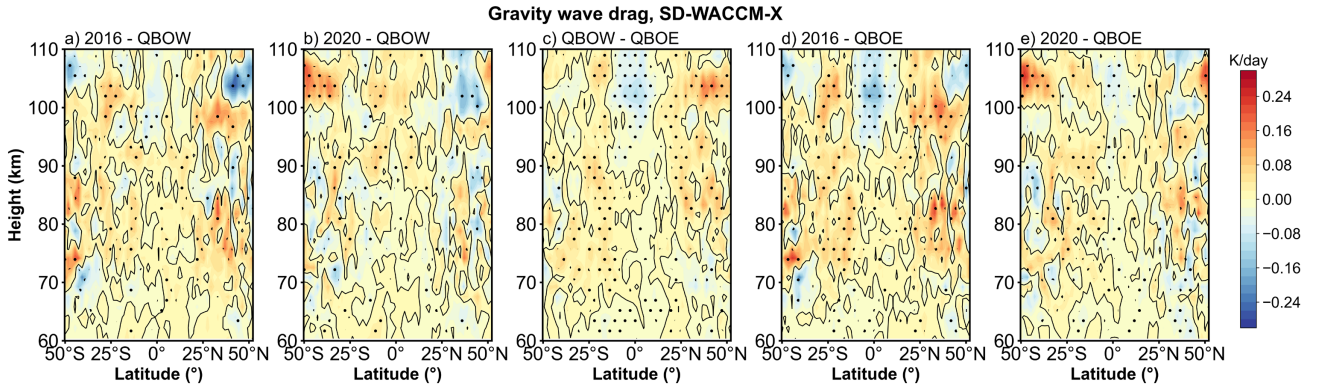
522 4.3 Contribution of Tide-gravity wave interaction during the events

523 The mesospheric diurnal tides are also affected by the interaction with GWs (Liu and Hagan, 1998; Mayr et al., 1998;
 524 McLandress, 2002a; Li et al., 2009; Lu et al., 2012; Yang et al., 2018; Stober et al., 2021; Cen et al., 2022). These interactions
 525 can strongly modulate tidal amplitude and phase (Liu and Hagan, 1998; Lu et al., 2009; Li et al., 2009; Wang et al., 2024). In
 526 the mesosphere, gravity-wave drag may be linked to the QBO. As discussed in Wang et al. (2024), QBO-dependent zonal
 527 wind shear and associated zero-wind lines filter the upward-propagating gravity waves that can reach the mesosphere, making
 528 the gravity wave drag exhibit QBO-like features. In the tropical region of the mesosphere, due to the strong interaction between
 529 the GWs and the semi-annual oscillation (SAO) in zonal wind, the GWs in the mesosphere exhibit a weak QBO signature.
 530 QBO-related variations in GWs primarily exists in the mid-latitude mesosphere.

531 To quantify the GW forcing on the DW1, the methods of Yang et al. (2018) and Cen et al. (2022) are applied. The equation is:

$$532 \quad \text{GW}_{\text{forcing}} = \text{GW}_{\text{drag}} \cdot \cos(\omega \cdot (\phi_{\text{GW}} - (\phi_T - 6))) \quad (5)$$

533 Where the GW_{drag} is the DW1 amplitude of GW drag, ω is the $24/2\pi$, ϕ_{GW} is the DW1 phase of GW drag while ϕ_T is DW1
 534 amplitude of temperature.



535 **Figure 11. Similar to figure 2 but the difference of gravity wave forcing. (a-e) give the difference result derived from SD-WACCM-**
 536 **X.**

538 After calculating the GW forcing, the classification method described in Section 3.1 is applied. As shown in Figure D1, GW
 539 tends to damp the DW1 amplitude at nearly all latitudes above 105 km. Below ~105 km, the GWs tend to damp the DW1
 540 amplitude at the equator while enhancing it at subtropical latitudes. Differences exist in the amplitude of gravity wave drag
 541 between different QBO phases. Figure 11 shows the differences in GW forcing between QBO phases, with dots indicating
 542 regions exceeding the 95% significance level. During QBOW (Fig. 11c), the equatorial damping and subtropical enhancement

are stronger than during QBOE. During the 2016 QBO disruption event, the pattern closely resembles the QBOW–QBOE difference but exhibits a larger magnitude than QBOW (Fig. 11a). During the 2020 disruption event, the GW drag is similar to QBOW conditions and is stronger than in QBOE. These results suggest that GW forcing exerts a significant influence on the modulation of DW1 amplitudes across QBO phases and disruption events.

5 Summary

In this work, the response of global DW1 amplitudes and phases during QBO disruption events is investigated using SABER observation, MERRA-2 dataset and SD-WACCM-X simulation results from 2002 to 2023. Additionally, the underlying mechanisms associated with these events are explored. The findings are summarized as follows:

(1) There are clear differences in (1, 1) mode vertical phase structure and wavelengths between QBO westerly phases and easterly phases. The DW1 (1, 1) mode vertical phase structure and wavelengths during these two QBO disruption events are similar to those during QBO westerly phases.

(2) During the 2016 QBO disruption event, DW1 amplitudes are markedly enhanced relative to regular QBOE but remain lower than those during QBOW. In the mesosphere and lower thermosphere (MLT), the amplitudes increase by ~ 1.56 K ($\sim 20.5\%$) at the equator and ~ 0.54 K ($\sim 14.4\%$) at 30° N/S yet are smaller than those during QBOW by ~ 1.22 K ($\sim 10.2\%$) at the equator. A pronounced difference of the DW1 (1, 1) mode relative to QBOW and QBOE is also evident in the stratosphere, with amplitudes ~ 0.21 K ($\sim 21\%$) higher than during QBOE and ~ 0.15 K ($\sim 10.9\%$) weaker than during QBOW.

By contrast, the 2020 disruption shows only a modest rise in DW1 amplitude relative to the regular QBOE and remain much weaker than during QBOW. In the MLT, the amplitudes rise by ~ 0.50 K ($\sim 6.0\%$) at the equator and ~ 0.26 K ($\sim 7.7\%$) at 30° N/S compared to QBOE, but are smaller than those during QBOW by 2.3 K ($\sim 21.1\%$) and 0.57 K ($\sim 12.0\%$), respectively. In the stratosphere, the amplitudes are about 0.18 K ($\sim 17.0\%$) larger than during QBOE but ~ 0.18 K ($\sim 12.5\%$) lower than during QBOW.

(3) During the 2016 event, the stronger water vapour radiative heating ($\sim 8.3\%$ relative to QBOE and $\sim 10.9\%$ relative to QBOW) and latent heating (22% relative to both QBO phases) enhance the tides at their source region. The enhanced water vapour radiative heating is jointly modulated by 2016 QBO disruption and 2015/16 El Niño event, whereas the enhanced latent heating is mainly due to the 2015/16 El Niño event. Weak dissipation (zonal winds) and less tidal energy removal (zonal wind latitudinal shear) during the tide propagate upward in the lower stratosphere do not tend to suppress DW1 amplitudes, while gravity waves strengthen DW1 in the subtropics and damp it at the equator. Nevertheless, a stronger shear near ~ 40 km likely prevents DW1 amplitudes from reaching the levels observed during normal QBO westerly phases. Overall, the joint modulation of water-vapor radiative heating, latent heating, weak dissipation, weak energy removal and positive GW drag contribute to a significant increase in DW1 amplitudes.

In contrast, during the 2020 event, only water vapour radiative heating exhibits a clear rise ($\sim 5\%$). The dissipation and the tidal energy removal in the stratosphere become larger, effectively suppressing DW1 enhancement. The gravity-wave effect

575 was weaker than in 2016 but still stronger than in QBOE. Consequently, the combined influence of water-vapor radiative
 576 heating and GW drag contribute to a slight increase in DW1 amplitudes relative to QBOE.
 577 This work analyzes how the DW1 varies when the highly unusual wind of QBO occurs. This phenomenon which is found in
 578 responses at different atmospheric layers suggests an atmosphere coupling process. The observations and model simulations
 579 give clear evidence of the connection. The possible link between the lower atmosphere trace gases variation and MLT dynamic
 580 features is shown during these unique events. The result gives a window for exploring the mechanism of the coupling,
 581 providing a basis for future research on the underlying mechanisms.

582 **Appendix A: approach for calculating the water vapor radiative heating rate**

583 The heating rate for water vapor mainly follows the method from Groves et al. (1982) and Lieberman et al. (2003).
 584 As mentioned in equation 1, the heating rate could be categorized into clear sky and cloudy sky. The equation of clear
 585 sky is given by Lacis and Hansen (1974):

$$586 \quad J_{clr} = q\eta^c S_0 \cos \zeta \left[MA(y) + \frac{5}{3} RA(y') \right] \quad (A1)$$

587 with q is water vapor mixing ratio (specific humidity), η is defined as p/p_0 , c is defined as $0.75 - \Gamma R_M/2g$. Γ is the
 588 vertical lapse rate, which is 6.5K km^{-1} . R_M is the gas constant for air. g is the acceleration of gravity. S_0 is the solar
 589 constant, which is 1353 W m^{-2} . ζ is the solar zenith angle, the equation is:

$$590 \quad \cos \zeta = \sin \theta \sin \delta + \cos \theta \cos \delta \cos t' \quad (A2)$$

591 with θ is the latitude, δ is the solar declination. t' is given by following equation:

$$592 \quad t' = \lambda + \Omega t \quad (A3)$$

593 with λ is longitude in radian, Ω is the angular frequency of Earth's rotation. t is the universal time.

594 M is given by equation:

$$595 \quad M = \frac{35}{(1224 \cos^2 \zeta + 1)^{\frac{1}{2}}} \quad (A4)$$

596 $A(y)$ is given by equation:

$$597 \quad A(y) = 2.9 \left[\frac{0.635 + 0.365Y}{(Y^{0.635} + 5.925y)^2 Y^{0.365}} \right] \text{cm}^2 \text{g}^{-1} \quad (A5)$$

598

599 with:

$$600 \quad Y = 1 + 141.5y \quad (A6)$$

601 and

$$602 \quad y = M\bar{w} \quad (A7)$$

603 and

$$604 \quad y' = M\bar{w}_t + \frac{5}{3}(\bar{w}_t - \bar{w}) \quad (A8)$$

605 The \bar{w} is the effective water vapor amount, is given by equation:

$$606 \quad \bar{w} = \int_z^\infty q\rho(p/p_0)^{.75}(T_0/T)^{1/2}dz \quad (A9)$$

607 Where ρ is the air density. \bar{w}_t is the total water vapor above the reflecting surface.

608 The cloudy sky heating rate is given by Groves (1982):

$$609 \quad J_{cla} = q\eta^c S_0 \cos \zeta Z \quad (A10)$$

610 with Z is parameter given by:

$$611 \quad Z = \sum_i \{ak'[\cosh(\xi_0 + \beta - \xi)) - \cosh(\xi_0 + \beta' - \xi)]/\sinh(\xi_0 + \beta)\}_i \quad (A11)$$

612 with ξ is given by:

$$613 \quad \xi = k'\bar{w} \quad (A12)$$

$$614 \quad k' = \frac{5}{3}\alpha(\sigma + k) \quad (A13)$$

615 with α , β and β' :

$$616 \quad \alpha = (1 - \omega)^{\frac{1}{2}}(1 + \omega - 2\omega f)^{\frac{1}{2}} \quad (A14)$$

$$617 \quad \beta = \frac{1}{2}\ln\{[1 + \alpha - \omega f - R\omega(1 - f)] \div [1 - \alpha - \omega f - R\omega(1 - f)]\} \quad (A15)$$

$$618 \quad \beta' = \beta + \frac{1}{2}\ln\left[\frac{1 - \alpha - \omega f}{1 + \alpha - \omega f}\right] \quad (A16)$$

619 with single scattering albedo:

$$620 \quad \omega = \frac{\sigma}{\sigma + k} \quad (A17)$$

621 where $\sigma = 40 \text{ cm}^{-1}$, f is 0.925, k and a are given by table 2 from Somerville et al. (1974).

622 **Appendix B: approach for calculating the ozone radiative heating rate**

623 The heating rate for ozone mainly uses the equations from Strobel/Zhu model (Strobel, 1978; Zhu, 1999) and processing
624 method from Xu et al. (2010). The Chappius, Hartley and Huggins bands are as follow:

$$625 \quad \frac{H_{\text{Ch}}}{[\text{O}_3]} = F_c \sigma_c \exp[-\sigma_c N_3] \quad (B1)$$

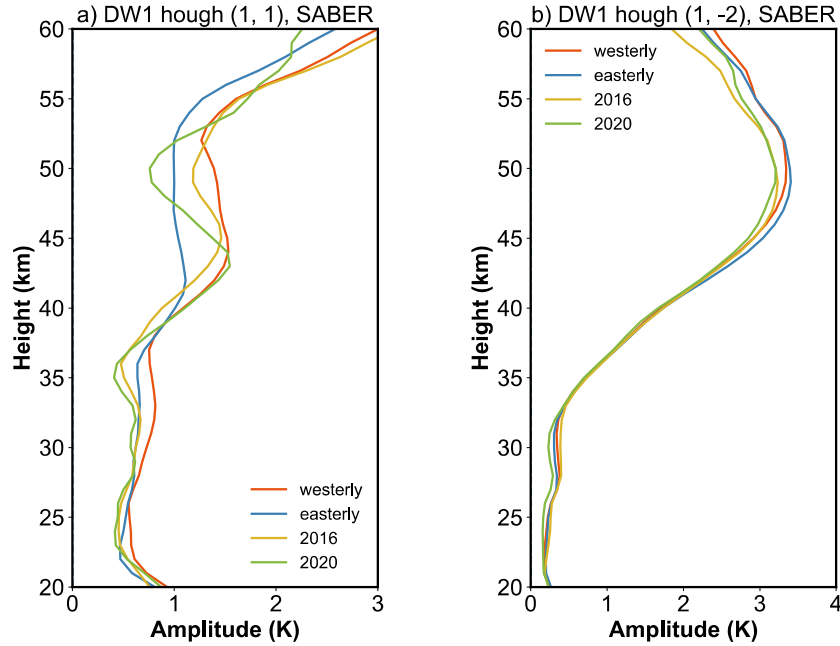
$$626 \quad \frac{H_{\text{Ha}}}{[\text{O}_3]} = F_{\text{Ha}} \sigma_{\text{Ha}} \exp[-\sigma_{\text{Ha}} N_3] \quad (B2)$$

$$\frac{H_{Hu}}{[O_3]} = \frac{1}{MN_3} \{I_1 + (I_2 - I_1) \exp[-\sigma_{Hu} N_3 e^{-M\lambda_{long}}] - I_2 \exp[-\sigma_{Hu} N_3 e^{-M\lambda_{short}}]\} \quad (B3)$$

628 The $[O_3]$ is the ozone number density while the N_3 is the column density of O_3 along the solar radiation path. For
629 equation B1, the F_c is $370 \text{ J m}^{-2} \text{ s}^{-1}$, the σ_c is 2.85×10^{-25} . For equation B2, the F_{Ha} is $5.13 \text{ J m}^{-2} \text{ s}^{-1}$, the σ_{Ha} is $8.7 \times 10^{-22} \text{ m}^{-2}$. For equation B3, the I_1 is $0.07 \text{ J m}^{-2} \text{ s}^{-1} \text{ \AA}^{-1}$, the I_2 is $0.07 \text{ J m}^{-2} \text{ s}^{-1} \text{ \AA}^{-1}$, M is 0.01273 \AA^{-1} , λ_{long} is 2805 \AA^{-1} , λ_{short}
630 is 3015 \AA^{-1} , σ_{Hu} is $1.15 \times 10^{-6} \text{ m}^{-2}$.
632 For the heating rate calculation, the ozone density profiles are firstly interpolated to a uniform vertical grid with 1 km spacing
633 from 20 km to 105 km. Then the ozone profiles are processing into zonal mean overlapping latitude bins that are 10 degrees
634 wide with centres offset by 5° from 50°S - 50°N . The diurnal variation of the vertical profile of the ozone heating rate in each
635 latitude bin is calculated using the SABER ozone density and equation B1-B3, along with the diurnal variation of solar zenith
636 angle for the specific latitude and day of year.

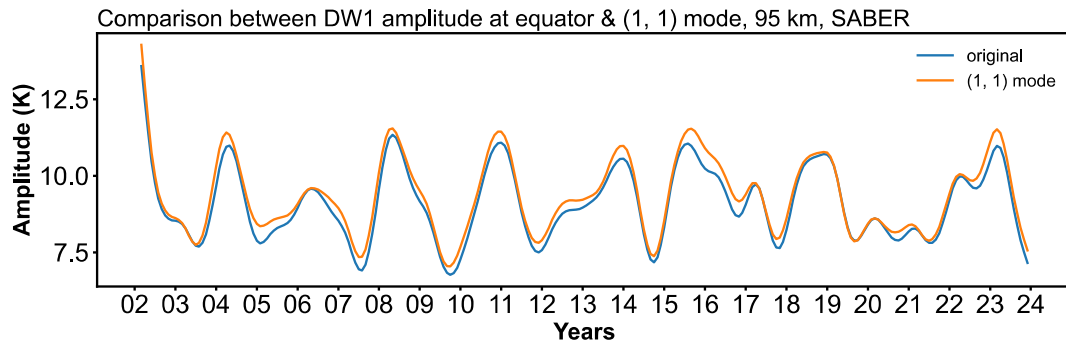
637 Appendix C: The feature of DW1 (1, 1) Hough mode

638

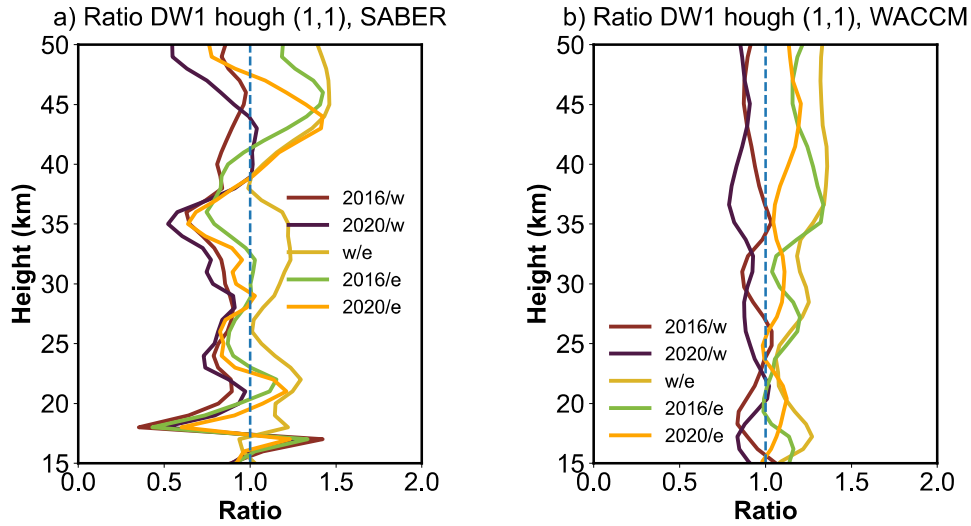


639

640 Figure C1. Amplitude profiles of DW1a) (1,1) and b) (1, -2) modes during different QBO phases



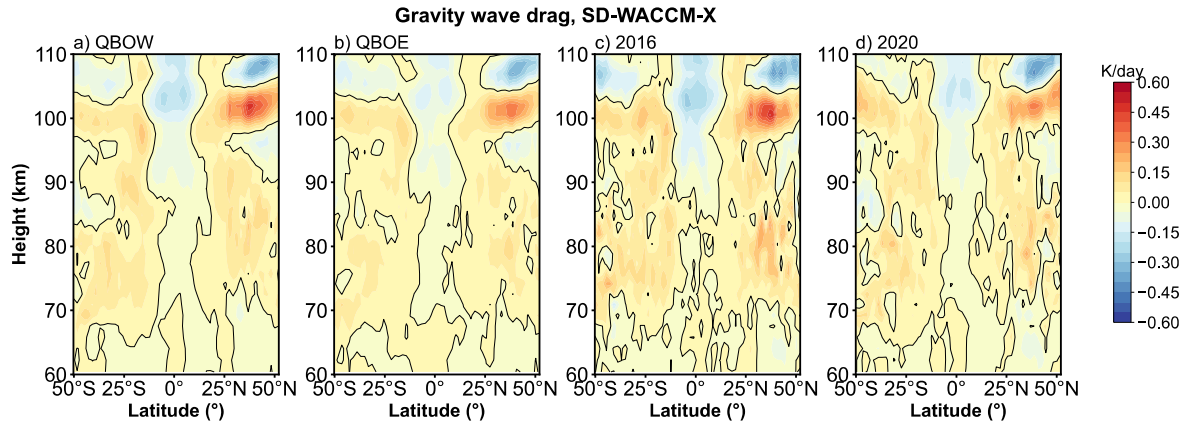
641
642 Figure C2. The amplitude time series of equatorial DW1 and (1, 1) Hough mode at 95 km.



643
644 Figure C3. the vertical profile of DW1 (1, 1) mode amplitude ratio derived from 2016/westerly (dark red), 2020/westerly (dark
645 purple), westerly/easterly (yellow), 2016/easterly (green), and 2020/easterly (orange). The dashed blue lines represent the ratio
646 of 1.
647

648 Appendix D: Gravity wave drag effect to DW1

649



650

651 Figure D1. The gravity wave forcing on DW1 during difference QBO phases as a function of latitude and altitude

652

653 **Data availability.** SABER data is available from the SABER project data server at
654 <https://spdf.gsfc.nasa.gov/pub/data/timed/saber/>. The SD-WACCM-X is retrieved from [https://app.globus.org/file-](https://app.globus.org/file-manager?origin_id=d2762023-6ab4-46c9-ab12-b037cd568e42&origin_path=%2F)
655 [manager?origin_id=d2762023-6ab4-46c9-ab12-b037cd568e42&origin_path=%2F](https://app.globus.org/file-manager?origin_id=d2762023-6ab4-46c9-ab12-b037cd568e42&origin_path=%2F). The QBO index is retrieved from
656 https://acd-ext.gsfc.nasa.gov/Data_services/met/qbo/QBO_Singapore_Uvals_GSFC.txt. The Generalized Lomb-
657 Scargle Periodogram and best-frequency fit method are provided by PyAstronomy
658 (<https://github.com/sczesla/PyAstronomy>). The MERRA-2 reanalysis data can be retrieved from
659 https://disc.gsfc.nasa.gov/datasets/M2T3NVASM_5.12.4/summary/ (zonal wind, temperature, cloud fraction, specific
660 humidity), https://disc.gsfc.nasa.gov/datasets/M2I3NVAER_5.12.4/summary (air density),
661 https://disc.gsfc.nasa.gov/datasets/M2T1NXRAD_5.12.4/summary (surface albedo),
662 https://disc.gsfc.nasa.gov/datasets/M2T3NPTDT_5.12.4/summary?keywords=MERRA2%20tdt (tendency of air
663 temperature due to moist processes).

664 **Author contributions.** Conceptualization: SL, GYJ; investigation: SL, GYJ; project administration:
665 BXL, GYJ and YJZ; software: SL; supervision: GYJ, BXL and YJZ; validation: BXL, GYJ and YJZ; visualization: SL;
666 writing – original draft preparation: SL; and writing – review and editing: GYJ, BXL, XL, JYX, YJZ and WY. All authors
667 have read and agreed to the published version of the paper.

668

669 **Competing interests.** The authors declare that they have no conflict of interest.

670

671 **Disclaimer.** Publisher's note: Copernicus Publications remains neutral with regard to jurisdictional claims made in the
672 text, published maps, institutional affiliations, or any other geographical representation in this paper. While Copernicus
673 Publications makes every effort to include appropriate place names, the final responsibility lies with the authors.

675 **Acknowledgements.** WACCM-X SD output data have been used in this study, and we would like to acknowledge the
676 WACCM-X development group at NCAR/HAO for making the model output publicly available. This work was jointly
677 supported by the Strategic Priority Research Program of the Chinese Academy of Sciences (Grant No. XDB0560000),
678 the Pandeng Program of National Space Science Center CAS, National Key R&D program of China (2023YFB3905100),
679 the Project of Stable Support for Youth Team in Basic Research Field, CAS (YSBR-018), the National Natural Science
680 Foundation of China (42174212), the Chinese Meridian Project, and the Specialized Research Fund for State Key
681 Laboratories.

682

683 **Financial support.** This work was jointly supported by the Strategic Priority Research Program of the Chinese Academy
684 of Sciences (Grant No. XDB0560000), the Pandeng Program of National Space Science Center CAS, National Key
685 R&D program of China (2023YFB3905100), the Project of Stable Support for Youth Team in Basic Research Field,
686 CAS (YSBR-018), the National Natural Science Foundation of China (42174212), the Chinese Meridian Project, and
687 the Specialized Research Fund for State Key Laboratories.

688

689 **References**

690 Anstey, J. A., Banyard, T. P., Butchart, N., Coy, L., Newman, P. A., Osprey, S., and Wright, C. J.: Prospect of Increased
691 Disruption to the QBO in a Changing Climate, *Geophys. Res. Lett.*, 48, 10.1029/2021gl093058, 2021.

692 Baldwin, M. P., Gray, L. J., Dunkerton, T. J., Hamilton, K., Haynes, P. H., Randel, W. J., Holton, J. R., Alexander, M. J.,
693 Hirota, I., Horinouchi, T., Jones, D. B. A., Kinniersley, J. S., Marquardt, C., Sato, K., and Takahashi, M.: The quasi-biennial
694 oscillation, *Rev. Geophys.*, 39, 179-229, 10.1029/1999rg000073, 2001.

695 Barton, C. A. and McCormack, J. P.: Origin of the 2016 QBO Disruption and Its Relationship to Extreme El Niño Events,
696 *Geophys. Res. Lett.*, 44, 10.1002/2017gl075576, 2017.

697 Cen, Y., Yang, C., Li, T., Russell Iii, J. M., and Dou, X.: Suppressed migrating diurnal tides in the mesosphere and lower
698 thermosphere region during El Niño in northern winter and its possible mechanism, *Atmos. Chem. Phys.*, 22, 7861-7874,
699 10.5194/acp-22-7861-2022, 2022.

700 Chapman, S. and Lindzen, R.: *Atmospheric tides – thermal and gravitational*, D. Reidel Publishing Company, Dordrecht, the
701 Netherlands, ISBN 978-94-010-3401-2, 1970.

702 Coy, L., Newman, P. A., Pawson, S., and Lait, L. R.: Dynamics of the Disrupted 2015/16 Quasi-Biennial Oscillation, *J. Clim.*,
703 30, 5661-5674, 10.1175/jcli-d-16-0663.1, 2017.

704 Davis, R. N., Du, J., Smith, A. K., Ward, W. E., and Mitchell, N. J.: The diurnal and semidiurnal tides over Ascension Island
 705 ($^{\circ}$ S, 14° W) and their interaction with the stratospheric quasi-biennial oscillation: studies with meteor radar, eCMAM and
 706 WACCM, *Atmos. Chem. Phys.*, 13, 9543-9564, 10.5194/acp-13-9543-2013, 2013.

707 de Araújo, L. R., Lima, L. M., Jacobi, C., and Batista, P. P.: Quasi-biennial oscillation signatures in the diurnal tidal winds
 708 over Cachoeira Paulista, Brazil, *J. Atmos. Sol. Terr. Phys.*, 155, 71-78, 10.1016/j.jastp.2017.02.001, 2017.

709 Dhadly, M. S., Emmert, J. T., Drob, D. P., McCormack, J. P., and Niciejewski, R. J.: Short-Term and Interannual Variations
 710 of Migrating Diurnal and Semidiurnal Tides in the Mesosphere and Lower Thermosphere, *J. Geophys. Res.: Space Phys.*, 123,
 711 7106-7123, 10.1029/2018ja025748, 2018.

712 Diallo, M., Riese, M., Birner, T., Konopka, P., Müller, R., Hegglin, M. I., Santee, M. L., Baldwin, M., Legras, B., and Ploeger,
 713 F.: Response of stratospheric water vapor and ozone to the unusual timing of El Niño and the QBO disruption in 2015–2016,
 714 *Atmos. Chem. Phys.*, 18, 13055-13073, 10.5194/acp-18-13055-2018, 2018.

715 Diallo, M. A., Ploeger, F., Hegglin, M. I., Ern, M., Grooß, J.-U., Khaykin, S., and Riese, M.: Stratospheric water vapour and
 716 ozone response to the quasi-biennial oscillation disruptions in 2016 and 2020, *Atmos. Chem. Phys.*, 22, 14303-14321,
 717 10.5194/acp-22-14303-2022, 2022.

718 Ern, M., Ploeger, F., Preusse, P., Gille, J. C., Gray, L. J., Kalisch, S., Mlynyczak, M. G., Russell, J. M., and Riese, M.: Interaction
 719 of gravity waves with the QBO: A satellite perspective, *J. Geophys. Res.: Atmos.*, 119, 2329-2355, 10.1002/2013jd020731,
 720 2014.

721 Forbes, J. M. and Vincent, R. A.: Effects of mean winds and dissipation on the diurnal propagating tide: An analytic approach,
 722 *Planet. Space Sci.*, 37, 197-209, 10.1016/0032-0633(89)90007-x, 1989.

723 Forbes, J. M. and Garrett, H. B.: Seasonal-Latitudinal Structure of the Diurnal Thermospheric Tide, *J. Atmos. Sci.*, 35, 148-
 724 159, 10.1175/1520-0469(1978)035<0148:Slstod>2.0.Co;2, 1978.

725 Gan, Q., Du, J., Ward, W. E., Beagley, S. R., Fomichev, V. I., and Zhang, S.: Climatology of the diurnal tides from eCMAM30
 726 (1979 to 2010) and its comparison with SABER, *Earth Planets Space*, 66, 10.1186/1880-5981-66-103, 2014.

727 Garcia, R. R.: On the Structure and Variability of the Migrating Diurnal Temperature Tide Observed by SABER, *J. Atmos.*
 728 *Sci.*, 80, 687-704, 10.1175/jas-d-22-0167.1, 2023.

729 Garcia, R. R., Marsh, D. R., Kinnison, D. E., Boville, B. A., and Sassi, F.: Simulation of secular trends in the middle atmosphere,
 730 1950–2003, *J. Geophys. Res.: Atmos.*, 112, 10.1029/2006jd007485, 2007.

731 Gelaro, R., McCarty, W., Suarez, M. J., Todling, R., Molod, A., Takacs, L., Randles, C., Darmenov, A., Bosilovich, M. G.,
 732 Reichle, R., Wargan, K., Coy, L., Cullather, R., Draper, C., Akella, S., Buchard, V., Conaty, A., da Silva, A., Gu, W., Kim, G.
 733 K., Koster, R., Lucchesi, R., Merkova, D., Nielsen, J. E., Partyka, G., Pawson, S., Putman, W., Rienecker, M., Schubert, S. D.,
 734 Sienkiewicz, M., and Zhao, B.: The Modern-Era Retrospective Analysis for Research and Applications, Version 2 (MERRA-
 735 2), *J Clim*, Volume 30, 5419-5454, 10.1175/JCLI-D-16-0758.1, 2017.

736 Groves, G. V.: Hough components of water vapour heating, *J. Atmos. Terr. Phys.*, 44, 281-290, 10.1016/0021-9169(82)90033-
 737 2, 1982.

738 Hagan, M. E.: Comparative effects of migrating solar sources on tidal signatures in the middle and upper atmosphere, J.
739 Geophys. Res.: Atmos., 101, 21213-21222, 10.1029/96jd01374, 1996.

740 Hagan, M. E., Burrage, M. D., Forbes, J. M., Hackney, J., Randel, W. J., and Zhang, X.: QBO effects on the diurnal tide in the
741 upper atmosphere, Earth Planets Space, 51, 571-578, 10.1186/BF03353216, 1999.

742 Holton, J. R. and Lindzen, R. S.: An Updated Theory for the Quasi-Biennial Cycle of the Tropical Stratosphere, J. Atmos. Sci.,
743 29, 1076-1080, 10.1175/1520-0469(1972)029<1076:Autftq>2.0.Co;2, 1972.

744 Hu, S. and Fedorov, A. V.: The extreme El Niño of 2015–2016 and the end of global warming hiatus, Geophys. Res. Lett., 44,
745 3816-3824, 10.1002/2017gl072908, 2017.

746 Jiang, G., Xu, J., Shi, J., Yang, G., Wang, X., and Yan, C.: The first observation of the atmospheric tides in the mesosphere
747 and lower thermosphere over Hainan, China, Chin. Sci. Bull., 55, 1059-1066, 10.1007/s11434-010-0084-8, 2010.

748 Johnston, B. R., Randel, W. J., and Braun, J. J.: Interannual Variability of Tropospheric Moisture and Temperature and
749 Relationships to ENSO Using COSMIC-1 GNSS-RO Retrievals, J. Clim., 35, 7109-7125, 10.1175/jcli-d-21-0884.1, 2022.

750 Kang, M.-J. and Chun, H.-Y.: Contributions of equatorial waves and small-scale convective gravity waves to the 2019/20
751 quasi-biennial oscillation (QBO) disruption, Atmos. Chem. Phys., 21, 9839-9857, 10.5194/acp-21-9839-2021, 2021.

752 Kang, M.-J., Chun, H.-Y., Son, S.-W., Garcia, R. R., An, S.-I., and Park, S.-H.: Role of tropical lower stratosphere winds in
753 quasi-biennial oscillation disruptions, Sci. Adv., 8, 10.1126/sciadv.abm7229, 2022.

754 Kogure, M. and Liu, H.: DW1 Tidal Enhancements in the Equatorial MLT During 2015 El Niño: The Relative Role of Tidal
755 Heating and Propagation, J. Geophys. Res.: Space Phys., 126, 10.1029/2021ja029342, 2021.

756 Kogure, M., Liu, H., and Jin, H.: Impact of Tropospheric Ozone Modulation Due To El Niño on Tides in the MLT, Geophys.
757 Res. Lett., 50, 10.1029/2023gl102790, 2023.

758 Lacis, A. A. and Hansen, J.: A Parameterization for the Absorption of Solar Radiation in the Earth's Atmosphere, J. Atmos.
759 Sci., 31, 118-133, 10.1175/1520-0469(1974)031<0118:Apftao>2.0.Co;2, 1974.

760 Li, T., She, C. Y., Liu, H. L., Yue, J., Nakamura, T., Krueger, D. A., Wu, Q., Dou, X., and Wang, S.: Observation of local
761 tidal variability and instability, along with dissipation of diurnal tidal harmonics in the mesopause region over Fort Collins,
762 Colorado (41°N, 105°W), J. Geophys. Res.: Atmos., 114, 10.1029/2008jd011089, 2009.

763 Lieberman, R. S., Ortland, D. A., and Yarosh, E. S.: Climatology and interannual variability of diurnal water vapor heating, J.
764 Geophys. Res.: Atmos., 108, 10.1029/2002jd002308, 2003.

765 Lieberman, R. S., Riggan, D. M., Ortland, D. A., Nesbitt, S. W., and Vincent, R. A.: Variability of mesospheric diurnal tides
766 and tropospheric diurnal heating during 1997–1998, J. Geophys. Res., 112, 10.1029/2007jd008578, 2007.

767 Lindzen, R. S. and Holton, J. R.: A Theory of the Quasi-Biennial Oscillation, J. Atmos. Sci., 25, 1095-1107, 10.1175/1520-
768 0469(1968)025<1095:Atotqb>2.0.Co;2, 1968.

769 Liu, G., Lieberman, R. S., Harvey, V. L., Pedatella, N. M., Oberheide, J., Hibbins, R. E., Espy, P. J., and Janches, D.: Tidal
770 Variations in the Mesosphere and Lower Thermosphere Before, During, and After the 2009 Sudden Stratospheric Warming,
771 J. Geophys. Res.: Space Phys., 126, 10.1029/2020ja028827, 2021.

772 Liu, H. L. and Hagan, M. E.: Local heating/cooling of the mesosphere due to gravity wave and tidal coupling, *Geophys. Res.*
 773 *Lett.*, 25, 2941-2944, 10.1029/98gl02153, 1998.

774 Liu, H. L., Bardeen, C. G., Foster, B. T., Lauritzen, P., Liu, J., Lu, G., Marsh, D. R., Maute, A., McInerney, J. M., Pedatella,
 775 N. M., Qian, L., Richmond, A. D., Roble, R. G., Solomon, S. C., Vitt, F. M., and Wang, W.: Development and Validation of
 776 the Whole Atmosphere Community Climate Model With Thermosphere and Ionosphere Extension (WACCM - X 2.0), *J. Adv.*
 777 *Model. Earth Syst.*, 10, 381-402, 10.1002/2017ms001232, 2018.

778 Liu, H. L., Foster, B. T., Hagan, M. E., McInerney, J. M., Maute, A., Qian, L., Richmond, A. D., Roble, R. G., Solomon, S.
 779 C., Garcia, R. R., Kinnison, D., Marsh, D. R., Smith, A. K., Richter, J., Sassi, F., and Oberheide, J.: Thermosphere extension
 780 of the Whole Atmosphere Community Climate Model, *J. Geophys. Res.: Space Phys.*, 115, 10.1029/2010ja015586, 2010.

781 Liu, M., Xu, J., Liu, H., and Liu, X.: Possible modulation of migrating diurnal tide by latitudinal gradient of zonal wind
 782 observed by SABER/TIMED, *Science China Earth Sciences*, 59, 408-417, 10.1007/s11430-015-5185-4, 2015.

783 Liu, S., Jiang, G., Luo, B., Xu, J., Lin, R., Zhu, Y., and Liu, W.: Solar Cycle Dependence of Migrating Diurnal Tide in the
 784 Equatorial Mesosphere and Lower Thermosphere, *Remote Sens.*, 16, 10.3390/rs16183437, 2024a.

785 Liu, Y., Xu, J., Smith, A. K., and Liu, X.: Seasonal and Interannual Variations of Global Tides in the Mesosphere and Lower
 786 Thermosphere Neutral Winds: I. Diurnal Tides, *J. Geophys. Res.: Space Phys.*, 129, 10.1029/2023ja031887, 2024b.

787 Lu, X., Liu, H. L., Liu, A. Z., Yue, J., McInerney, J. M., and Li, Z.: Momentum budget of the migrating diurnal tide in the
 788 Whole Atmosphere Community Climate Model at vernal equinox, *J. Geophys. Res.: Atmos.*, 117, n/a-n/a,
 789 10.1029/2011jd017089, 2012.

790 Lu, X., Liu, A. Z., Swenson, G. R., Li, T., Leblanc, T., and McDermid, I. S.: Gravity wave propagation and dissipation from
 791 the stratosphere to the lower thermosphere, *J. Geophys. Res.: Atmos.*, 114, 10.1029/2008jd010112, 2009.

792 Marsh, D. R., Mills, M. J., Kinnison, D. E., Lamarque, J.-F., Calvo, N., and Polvani, L. M.: Climate Change from 1850 to
 793 2005 Simulated in CESM1(WACCM), *J. Clim.*, 26, 7372-7391, 10.1175/jcli-d-12-00558.1, 2013.

794 Mayr, H. G., Mengel, J. G., Talaat, E. R., Porter, H. S., and Chan, K. L.: Mesospheric non-migrating tides generated with
 795 planetary waves: I. Characteristics, *J. Atmos. Sol. Terr. Phys.*, 67, 959-980, 10.1016/j.jastp.2005.03.002, 2005.

796 Mayr, H. G., Mengel, J. G., Chan, K. L., and Porter, H. S.: Seasonal variations of the diurnal tide induced by gravity wave
 797 filtering, *Geophys. Res. Lett.*, 25, 943-946, 10.1029/98gl00637, 1998.

798 McLandress, C.: The Seasonal Variation of the Propagating Diurnal Tide in the Mesosphere and Lower Thermosphere. Part I:
 799 The Role of Gravity Waves and Planetary Waves, *J. Atmos. Sci.*, 59, 893-906, 10.1175/1520-
 800 0469(2002)059<0893:Tsvotp>2.0.Co;2, 2002a.

801 McLandress, C.: The Seasonal Variation of the Propagating Diurnal Tide in the Mesosphere and Lower Thermosphere. Part
 802 II: The Role of Tidal Heating and Zonal Mean Winds, *J. Atmos. Sci.*, 59, 907-922, 10.1175/1520-
 803 0469(2002)059<0907:Tsvotp>2.0.Co;2, 2002b.

804 Mertens, C. J.: SABER observations of mesospheric temperatures and comparisons with falling sphere measurements taken
 805 during the 2002 summer MaCWAVE campaign, *Geophys. Res. Lett.*, 31, 10.1029/2003gl018605, 2004.

806 Mertens, C. J., Mlynczak, M. G., López-Puertas, M., Wintersteiner, P. P., Picard, R. H., Winick, J. R., Gordley, L. L., and
 807 Russell, J. M.: Retrieval of mesospheric and lower thermospheric kinetic temperature from measurements of CO₂ 15 μ m Earth
 808 Limb Emission under non-LTE conditions, *Geophys. Res. Lett.*, 28, 1391-1394, 10.1029/2000gl012189, 2001.
 809 Mlynczak, M. G., Hunt, L. A., Garcia, R. R., Harvey, V. L., Marshall, B. T., Yue, J., Mertens, C. J., and Russell, J. M., 3rd:
 810 Cooling and Contraction of the Mesosphere and Lower Thermosphere From 2002 to 2021, *J Geophys Res Atmos*, 127,
 811 e2022JD036767, 10.1029/2022JD036767, 2022.
 812 Mlynczak, M. G., Marshall, B. T., Garcia, R. R., Hunt, L., Yue, J., Harvey, V. L., Lopez-Puertas, M., Mertens, C., and Russell,
 813 J.: Algorithm Stability and the Long-Term Geospace Data Record From TIMED/SABER, *Geophys. Res. Lett.*, 50,
 814 10.1029/2022gl102398, 2023.
 815 Mukhtarov, P., Pancheva, D., and Andonov, B.: Global structure and seasonal and interannual variability of the migrating
 816 diurnal tide seen in the SABER/TIMED temperatures between 20 and 120 km, *J. Geophys. Res.: Space Phys.*, 114, n/a-n/a,
 817 10.1029/2008ja013759, 2009.
 818 Newman, P. A., Coy, L., Pawson, S., and Lait, L. R.: The anomalous change in the QBO in 2015-2016, *Geophys. Res. Lett.*,
 819 43, 8791-8797, 10.1002/2016gl070373, 2016.
 820 Neale, R., Richter, J. H., Conley, A. J., Park, S., Lauritzen, P. H., Gettelman, A., Williamson, D., Rasch, P. J., Vavrus, S. J.,
 821 Taylor, M. A., Collins, W., Zhang, M., & LIN, S. (2010). Description of the NCAR Community Atmosphere Model (CAM
 822 4.0), 10.5065/GSEB-6470, 2010
 823 Oberheide, J., Forbes, J. M., Häusler, K., Wu, Q., and Bruinsma, S. L.: Tropospheric tides from 80 to 400 km: Propagation,
 824 interannual variability, and solar cycle effects, *J. Geophys. Res.: Atmos.*, 114, 10.1029/2009jd012388, 2009.
 825 Ortland, D. A.: Daily estimates of the migrating tide and zonal mean temperature in the mesosphere and lower thermosphere
 826 derived from SABER data, *J. Geophys. Res.: Atmos.*, 122, 3754-3785, 10.1002/2016jd025573, 2017.
 827 Osprey, S. M., Butchart, N., Knight, J. R., Scaife, A. A., Hamilton, K., Anstey, J. A., Schenzinger, V., and Zhang, C.: An
 828 unexpected disruption of the atmospheric quasi-biennial oscillation, *Science*, 353, 1424-1427, 10.1126/science.aah4156, 2016.
 829 Pedatella, N.: Ionospheric Variability during the 2020–2021 SSW: COSMIC-2 Observations and WACCM-X Simulations,
 830 *Atmosphere*, 13, 10.3390/atmos13030368, 2022.
 831 Pramitha, M., Kishore Kumar, K., Venkat Ratnam, M., Praveen, M., and Rao, S. V. B.: Disrupted Stratospheric QBO
 832 Signatures in the Diurnal Tides Over the Low-Latitude MLT Region, *Geophys. Res. Lett.*, 48, 10.1029/2021gl093022, 2021a.
 833 Pramitha, M., Kumar, K. K., Ratnam, M. V., Praveen, M., and Bhaskara Rao, S. V.: Stratospheric Quasi Biennial Oscillation
 834 Modulations of Migrating Diurnal Tide in the Mesosphere and Lower Thermosphere Over the Low and Equatorial Latitudes,
 835 *J. Geophys. Res.: Space Phys.*, 126, 10.1029/2020ja028970, 2021b.
 836 Qian, L., Emery, B. A., Foster, B., Lu, G., Maute, A., Richmond, A. D., et al.: The NCAR TIE-GCM: A community model of
 837 the coupled thermosphere/ionosphere system. In J. Huba, R. Schunk, & G. Khazanov (Eds.), *Modeling the ionosphere-*
 838 *thermosphere system*, John Wiley, 73–83, 10.1002/9781118704417.ch7, 2014

839 Riggins, D. M. and Lieberman, R. S.: Variability of the diurnal tide in the equatorial MLT, *J. Atmos. Sol. Terr. Phys.*, 102, 198-
840 206, 10.1016/j.jastp.2013.05.011, 2013.

841 Sakazaki, T., Fujiwara, M., and Shiotani, M.: Representation of solar tides in the stratosphere and lower mesosphere in state-
842 of-the-art reanalyses and in satellite observations, *Atmos. Chem. Phys.*, 18, 1437-1456, 10.5194/acp-18-1437-2018, 2018.

843 Sakazaki, T., Fujiwara, M., and Zhang, X.: Interpretation of the vertical structure and seasonal variation of the diurnal
844 migrating tide from the troposphere to the lower mesosphere, *J. Atmos. Sol. Terr. Phys.*, 105-106, 66-80,
845 10.1016/j.jastp.2013.07.010, 2013.

846 Santoso, A., McPhaden, M. J., and Cai, W.: The Defining Characteristics of ENSO Extremes and the Strong 2015/2016 El
847 Niño, *Rev. Geophys.*, 55, 1079-1129, 10.1002/2017rg000560, 2017.

848 Schoeberl, M. R., Douglass, A. R., Newman, P. A., Lait, L. R., Lary, D., Waters, J., Livesey, N., Froidevaux, L., Lambert, A.,
849 Read, W., Filipiak, M. J., and Pumphrey, H. C.: QBO and annual cycle variations in tropical lower stratosphere trace gases
850 from HALOE and Aura MLS observations, *J. Geophys. Res.: Atmos.*, 113, 10.1029/2007jd008678, 2008.

851 Siddiqui, T. A., Chau, J. L., Stolle, C., and Yamazaki, Y.: Migrating solar diurnal tidal variability during Northern and Southern
852 Hemisphere Sudden Stratospheric Warmings, *Earth Planets Space*, 74, 10.1186/s40623-022-01661-y, 2022.

853 Singh, D. and Gurubaran, S.: Variability of diurnal tide in the MLT region over Tirunelveli (8.7°N), India: Consistency
854 between ground- and space-based observations, *J. Geophys. Res.: Atmos.*, 122, 2696-2713, 10.1002/2016jd025910, 2017.

855 Smith, A. K.: Global Dynamics of the MLT, *Surv. Geophys.*, 33, 1177-1230, 10.1007/s10712-012-9196-9, 2012.

856 Smith, A. K., Pedatella, N. M., Marsh, D. R., and Matsuo, T.: On the Dynamical Control of the Mesosphere–Lower
857 Thermosphere by the Lower and Middle Atmosphere, *J. Atmos. Sci.*, 74, 933-947, 10.1175/jas-d-16-0226.1, 2017.

858 Smith, A. K., Harvey, V. L., Mlynczak, M. G., Funke, B., García-Comas, M., Hervig, M., Kaufmann, M., Kyrölä, E., López-
859 Puertas, M., McDade, I., Randall, C. E., Russell, J. M., Sheese, P. E., Shiotani, M., Skinner, W. R., Suzuki, M., and Walker,
860 K. A.: Satellite observations of ozone in the upper mesosphere, *J. Geophys. Res.: Atmos.*, 118, 5803-5821, 10.1002/jgrd.50445,
861 2013.

862 Somerville, R. C. J., Stone, P. H., Halem, M., Hansen, J. E., Hogan, J. S., Druyan, L. M., Russell, G., Lacis, A. A., Quirk, W.
863 J., and Tenenbaum, J.: The GISS Model of the Global Atmosphere, *J. Atmos. Sci.*, 31, 84-117, 10.1175/1520-
864 0469(1974)031<0084:Tgmotg>2.0.Co;2, 1974.

865 Sun, R., Gu, S., Dou, X., and Li, N.: Tidal Structures in the Mesosphere and Lower Thermosphere and Their Solar Cycle
866 Variations, *Atmosphere*, 13, 10.3390/atmos13122036, 2022.

867 Stober, G., Kuchar, A., Pokhotelov, D., Liu, H., Liu, H.-L., Schmidt, H., Jacobi, C., Baumgarten, K., Brown, P., Janches, D.,
868 Murphy, D., Kozlovsky, A., Lester, M., Belova, E., Kero, J., and Mitchell, N.: Interhemispheric differences of mesosphere–
869 lower thermosphere winds and tides investigated from three whole-atmosphere models and meteor radar observations, *Atmos.*
870 *Chem. Phys.*, 21, 13855-13902, 10.5194/acp-21-13855-2021, 2021.

871 Strobel, D. F.: Parameterization of the atmospheric heating rate from 15 to 120 km due to O₂ and O₃ absorption of solar
872 radiation, *J. Geophys. Res.: Oceans*, 83, 6225-6230, 10.1029/JC083iC12p06225, 1978.

873 Tweedy, O. V., Kramarova, N. A., Strahan, S. E., Newman, P. A., Coy, L., Randel, W. J., Park, M., Waugh, D. W., and Frith,
874 S. M.: Response of trace gases to the disrupted 2015–2016 quasi-biennial oscillation, *Atmos. Chem. Phys.*, 17, 6813-6823,
875 10.5194/acp-17-6813-2017, 2017.

876 Vincent, R. A., Kovalam, S., Fritts, D. C., and Isler, J. R.: Long-term MF radar observations of solar tides in the low-latitude
877 mesosphere: Interannual variability and comparisons with the GSWM, *J. Geophys. Res.: Atmos.*, 103, 8667-8683,
878 10.1029/98jd00482, 1998.

879 Wang, J., Li, N., Yi, W., Xue, X., Reid, I. M., Wu, J., Ye, H., Li, J., Ding, Z., Chen, J., Li, G., Tian, Y., Chang, B., Wu, J., and
880 Zhao, L.: The impact of quasi-biennial oscillation (QBO) disruptions on diurnal tides over the low- and mid-latitude
881 mesosphere and lower thermosphere (MLT) region observed by a meteor radar chain, *Atmos. Chem. Phys.*, 24, 13299-13315,
882 10.5194/acp-24-13299-2024, 2024.

883 Wang, Y., Rao, J., Lu, Y., Ju, Z., Yang, J., and Luo, J.: A revisit and comparison of the quasi-biennial oscillation (QBO)
884 disruption events in 2015/16 and 2019/20, *Atmos. Res.*, 294, 10.1016/j.atmosres.2023.106970, 2023.

885 Wu, D. L., McLandress, C., Read, W. G., Waters, J. W., and Froidevaux, L.: Equatorial diurnal variations observed in UARS
886 Microwave Limb Sounder temperature during 1991–1994 and simulated by the Canadian Middle Atmosphere Model, *J.*
887 *Geophys. Res.: Atmos.*, 103, 8909-8917, 10.1029/98jd00530, 1998.

888 Wu, Q., Ortland, D. A., Killeen, T. L., Roble, R. G., Hagan, M. E., Liu, H. L., Solomon, S. C., Xu, J., Skinner, W. R., and
889 Niciejewski, R. J.: Global distribution and interannual variations of mesospheric and lower thermospheric neutral wind diurnal
890 tide: 1. Migrating tide, *J. Geophys. Res.: Space Phys.*, 113, n/a-n/a, 10.1029/2007ja012542, 2008.

891 Xu, J., Smith, A. K., Jiang, G., and Yuan, W.: Seasonal variation of the Hough modes of the diurnal component of ozone
892 heating evaluated from Aura Microwave Limb Sounder observations, *J. Geophys. Res.: Atmos.*, 115, 10.1029/2009jd013179,
893 2010.

894 Xu, J., Smith, A. K., Yuan, W., Liu, H. L., Wu, Q., Mlynczak, M. G., and Russell, J. M.: Global structure and long-term
895 variations of zonal mean temperature observed by TIMED/SABER, *J. Geophys. Res.*, 112, 10.1029/2007jd008546, 2007.

896 Xu, J., Smith, A. K., Liu, H. L., Yuan, W., Wu, Q., Jiang, G., Mlynczak, M. G., Russell, J. M., and Franke, S. J.: Seasonal and
897 quasi-biennial variations in the migrating diurnal tide observed by Thermosphere, Ionosphere, Mesosphere, Energetics and
898 Dynamics (TIMED), *J. Geophys. Res.*, 114, 10.1029/2008jd011298, 2009.

899 Yang, C., Smith, A. K., Li, T., and Dou, X.: The Effect of the Madden - Julian Oscillation on the Mesospheric Migrating
900 Diurnal Tide: A Study Using SD - WACCM, *Geophys. Res. Lett.*, 45, 5105-5114, 10.1029/2018gl077956, 2018.

901 Zhu, X.: An Accurate and Efficient Radiation Algorithm for Middle Atmosphere Models, *J. Atmos. Sci.*, 51, 3593-3614,
902 10.1175/1520-0469(1994)051<3593:Aaaera>2.0.Co;2, 1994.